

PAPER • OPEN ACCESS

Operational and plume properties of a modular hollow cathode for ground testing of plasma thrusters

To cite this article: Mohamed Ahmed et al 2025 J. Phys. D: Appl. Phys. 58 285204

View the article online for updates and enhancements.

You may also like

- The Electrochemical Performance of The Blended Cathode of LMFP and NMC811 Mutsuki Oikawa, Jun Ikegami, Yuma Shimbori et al
- Water Vapor Transport Measurement and Its Effect on Pemfcs Performance Ramesh Yadav, Greg DiLeo, Nilesh Dale et al.
- Selectivity of Diphenylacetylene Semi-Hydrogenation on Pt1Pd99/C Using PEM Electrolyzer

Hiroki Nakamura, Juri Harada, Naoki Shida et al.



J. Phys. D: Appl. Phys. 58 (2025) 285204 (21pp)

https://doi.org/10.1088/1361-6463/ade44f

Operational and plume properties of a modular hollow cathode for ground testing of plasma thrusters

Mohamed Ahmed^{1,*}, Mansur Tisaev², Silvia Masillo³ and Andrea Lucca Fabris

Surrey Space Centre, University of Surrey, Guildford, GU2 7XH, United Kingdom

E-mail: m.m.h.ahmed@soton.ac.uk

Received 15 February 2025, revised 25 May 2025 Accepted for publication 13 June 2025 Published 15 July 2025



Abstract

Hollow cathodes are widely used for spacecraft electric propulsion, however improved understanding of the cathode plasma plume is required to improve performance and lifetime. The modular hollow cathode is developed to assist in cost effective ground testing by allowing simplified component replacement in the case of failure. In this work, a Langmuir probe is employed to characterise the plasma potential, electron temperature and electron density in the external cathode plume. Additionally, optical emission spectroscopy is used to qualitatively infer the relative plume composition. We examine the plume through independent tests using xenon and krypton, adjusting mass flow rates and other operating parameters. The modular hollow cathode exhibits different modes of operation including plume, spot, and diffuse modes. The experimental observations align with the theoretical predictions using various plasma mode transition criteria. In particular, the predator-prey criterion based on the ratio between the discharge current and the mass flow rate captures most of the mode transitions. Xenon operation results in a higher current collected at the anode in comparison to krypton where the total discharge power increases. Measurements collected determine the variation of the plasma properties at a fixed position from the keeper as a function of mass flow rate, keeper current and anode voltage in a triode configuration. The plasma potential and electron temperature downstream of the cathode orifice decrease with increased mass flow rate due to a more collisional plasma. As the flow rate rises, and with it the collisionality of the cathode plasma, the trends in electron temperature align well with qualitative Xe neutral/ion line ratios. The cathode

Original Content from this work may be used under the terms of the Creative Commons Attribution 4.0 licence. Any further distribution of this work must maintain attribution to the author(s) and the title of the work, journal citation and DOI.

¹ Current affiliation: University of Southampton, Southampton, SO17 1BJ, United Kingdom.

² Current affiliation: Oregon State University, Corvallis, OR 97331, United States of America.

³ Current affiliation: Swissto12, Av. des Baumettes 9, 1020 Renens, Switzerland.

^{*} Author to whom any correspondence should be addressed.

is also coupled to a low-power wall-less (external discharge) hall thruster and operated on xenon to investigate the influence of the mode of operation on the discharge current and coupling voltage.

Keywords: hollow cathode neutraliser, modularity, plasma diagnostics, cathode plasma mode

Nomenclature

D_{p}	Outer diameter of the Langmuir probe (m)
$d_{\mathrm{o}}^{'}$	Orifice diameter of the cathode (m)
z	Axial distance of the probe to the keeper (m)
$n_{\rm n}$	Neutral density (m^{-3})
$\lambda_{ m e}$	Mean free path for elastic electron-neutral
	collisions
I_{k}	Keeper current (A)
$I_{\rm a}$	Anode current (A)
$I_{\rm d}$	Discharge current (A)
I_{probe}	Probe current collected (A)
I_{e}	Electron current (A)
$r_{ m p}$	Radius of the probe (m)
$V_{ m p}$	Plasma potential (V)
$n_{\mathrm{i/e}}$	Ion/Electron density (m ⁻³)
e	Elementary charge $(1.6 \times 10^{-19} \text{ C})$
$\lambda_{ m i}$	Ionisation mean free path (m)
$\sigma_{ m i}$	Average ionisation cross section (m ²)
$T_{ m g}$	Neutral temperature (eV or K)
$k_{ m B}$	Boltzmann constant $(1.38 \times 10^{-23} \text{ J K}^{-1})$
$v_{\rm n}$	Neutral velocity (m s ⁻¹)
$\dot{m}_{ m a}$	Thruster mass flow rate (kg s^{-1})
d_{p}	Inner diameter of the Langmuir probe (m)
$r_{ m k}$	Radius of the keeper orifice (m)
$\dot{m}_{ m c}$	Cathode mass flow rate (kg s ⁻¹)
$\sigma_{ m en}$	Average electron-neutral elastic collision cross
	section (m ²)
V_{k}	Keeper voltage (V)
V_{a}	Anode voltage (V)
$V_{ m C2G}$	Cathode-to-ground voltage (V)
$V_{ m Bias}$	Probe bias voltage (V)
$I_{i,sat}$	Ion saturation current (A)
$A_{\rm p}$	Area of the probe (m ²)
$\lambda_{ m D}$	Debye length (m)
$T_{i/e}$	Ion/Electron temperature (eV or K)
$m_{\rm e}$	Electron mass $(9.1 \times 10^{-31} \text{ kg})$
$M_{ m Xe/Kr}$	Ion mass Xe or Kr (kg)
$J_{ m o}$	Mass flow rate in equivalent ampere (A-equiv)
$W_{ m Xe/Kr}$	Propellant atomic mass Xe or Kr (amu)
$ u_{ m en}$	Electron-neutral collision frequency (Hz)
A_z	Cathode plume cross sectional area (m ²)
θ	Divergence half-angle of the cathode plume
_	(degrees or °)
D_{A}	Anode diameter (m)

1. Introduction

In various electric propulsion technologies such as hall effect and gridded ion thrusters, hollow cathodes are essential, serving both as discharge electron sources and ion beam neutralisers. These cathodes use low work-function materials like tungsten impregnated with barium oxide (BaO-W) or lanthanum hexaboride (LaB₆) as thermionic emitters to supply electrons to the plasma [1]. In conventional hollow cathodes, these materials are placed within a refractory metal or graphite cathode tube, heated resistively, and exposed to injected gas, creating a cathode plasma as emitted electrons ionise the gas. The entire setup is enclosed within a positively biased keeper electrode, initiating the cathode discharge, sustaining the plasma, protecting the core, reducing heat loss, and shielding against external plasma impacts [1, 2]. Due to its significant impact on various aspects of the hollow cathode, such as ignition, efficiency, and lifespan, extensive research has been conducted on keeper-related phenomena [3–7].

The modular hollow cathode design, featuring interchangeable parts, has been created to both streamline experimental troubleshooting and provide flexibility in the mechanical setup. It is characterised by direct contact between the heater assembly and the tungsten emitter impregnated with barium oxide, along with a ceramic spacer isolating the keeper electrode from the orifice disk [8]. Once the cathode ignites and operates with only the keeper active, it is observed that the cathode exhibits distinct plasma discharge modes - called the plume mode, the spot mode, and the diffuse mode – as a function of the mass flow rate and discharge current [8]. The spot mode is characterised by minor fluctuations in the voltage and current between the externally positioned anode, keeper, and cathode [9, 10]. It involves the formation of a small region of concentrated plasma, often referred to as 'spotlike' at the orifice whereas, in plume mode, the plume brightness and divergence increase due to the stretching of the ionisation and excitation regions away from the orifice [9, 10]. Additionally, at low mass flow rates and high anode current the plume brightness expands into the vacuum vicinity and that regime is categorised in literature as 'diffuse' mode [11, 12].

In literature [9, 12–17], the plume mode in general occurs during high discharge current to mass flow rate ratios and is characterised by significant fluctuations in both voltage and current between the keeper and the cathode, as well as between the anode and the cathode. Research examining the transitional characteristics of low current cathodes [10, 18] has revealed that, in plume mode, the discharge voltage tends to increase by several volts. Large plasma oscillations can be expected due to the production of energetic ions [4, 5, 18–22]. These energetic ions induce keeper erosion which can limit the lifetime of the cathode. The scientific community has been studying the cathode discharge modes and mode transition processes for many years to understand how cathodes switch between different operational states. The goal is to accurately

predict the regions where specific discharge modes occur, based on known cathode operational parameters. Despite various criteria proposed for mode transitions, there are different approaches regarding how cathodes precisely transition between spot and plume modes, as well as the fundamental physical processes that govern the operation of the plume mode, due to different geometric configurations and/or experimental characterisations. In previous work [8], the modular hollow cathode was shown to exhibit distinct plasma modes of operation; however, the underlying mechanisms driving transitions between these modes were not thoroughly characterised. The purpose of this study is to advance that initial development by systematically identifying the mode transition criteria using a combination of established theoretical criteria (e.g. Predatory-Prey, Kaufman, and Rehn-Kaufman), visual plume observations, Langmuir probe diagnostics, and optical emission spectroscopy (OES). This integrated approach enables quantification of key plasma parameters such as electron temperature, plasma potential, and density across different operating regimes. These results aim to provide a more complete understanding of the external plasma behaviour of the cathode, which is essential to improve ground testing procedures, validate simulation models, and guide future cathode designs for electric propulsion applications.

In this paper we also present the coupled operation of the modular hollow cathode with the external discharge plasma thruster (XPT). This device produces and sustains a plasma discharge completely in the open space outside the thruster body. The ionisation of neutrals and acceleration of ions takes place in a very narrow region near the anode surface [23, 24]. The thruster prototype is composed of a metal anode, a planar ceramic front wall, a pair of permanent magnets and the structure is composed of paramagnetic material. The modular hollow cathode is coupled with the XPT to quantify the impact of the cathode mode of operation on the discharge envelope, i.e. current-voltage profiles. The tested thruster-cathode configuration involves the cathode being externally mounted at 90° to the thruster's symmetry axis. This paper presents findings for anode voltages ranging from 100 V to 300 V and anode xenon mass flow rates of 0.5, 0.8, and $1.0 \,\mathrm{mg \, s^{-1}}$, with cathode xenon operation at 0.1 mg s^{-1} and 0.3 mg s^{-1} .

The article is organised as follows. Section 2 describes the geometric configuration of the modular cathode design along with the experimental apparatus and setup. Section 3 gives an overview of the experimental results in standalone and coupled operation with their conclusions. Specifically, section 3.1 provides an overview of the current-voltage characteristics in standalone diode mode operation, presents the results of the Langmuir probe measurements, and discusses the external plasma properties of the modular hollow cathode at different operating conditions, including various mass flow rates of xenon and krypton for multiple keeper currents. Section 3.2 presents the current-voltage characteristics in standalone triode mode operation, discusses the findings on the krypton and xenon plasma discharge parameters as the anode voltage is swept from 20 to 50 V, illustrates the plasma properties such as electron temperature, electron density and plasma potential as the mass flow rate is varied, and presents OES measurements at the keeper. The results from the investigation of coupling with the XPT, whether in spot or plume mode, are presented in section 3.3. Finally, the conclusions are presented in section 4.

2. Experimental characterisation

2.1. The modular hollow cathode

The modular hollow cathode is made up of four major components: the keeper disk, the orifice disk, the refractory metal heating element, and the insert (thermionic emitter). In figure 1, a sectional view of the modular hollow cathode is shown. The keeper disk has a diameter of 23 mm, a thickness of 2 mm, and a central hole of 2 mm. The radiation shield extends towards the base of the cathode 50 mm from the keeper disk. The keeper-to-orifice diameter ratio is 2, with the cathode orifice aspect ratio of 1. More detailed information on the dimensions can be found in [8].

The heating element consists of a rhenium wire wound through three concentric boron nitride (BN) ceramic cylinders, each featuring two azimuthally aligned rows of holes. The emitter is positioned between the orifice disk and the BN ceramic in direct contact with the heater assembly as shown in figure 1. To ensure the integrity of the assembly, mechanical fasteners are used. This construction allows for the replacement of individual components as needed, facilitating quick repairs or replacements of internal parts. Additionally, it can be adjusted to achieve the desired performance of the cathode by controlling the flow of current. The keeper disk is mounted to the orifice plate using ceramic spacers for electrical insulation and molybdenum fasteners, avoiding direct contact with the cathode base. More information on the design can be found in [8].

2.2. Operational envelope

The cathode's discharge characteristics are investigated in two configurations: diode mode (between cathode and keeper) and triode mode (cathode, keeper, and anode). These configurations, referred to as modes, are different from the plasma plume operational modes investigated in section 3.2.2. In both configurations, the discharge envelope is measured for multiple mass flow rates of xenon and krypton. The ignition is achieved with a heating power in the 95-120 W range. The operational specifications are presented in table 1. After ignition, the cathode only operates with the keeper active. Throughout the experiments, a fixed cathodeanode distance of 30 mm is maintained. For a concise summary of the various experimental campaigns and the respective test envelopes, please refer to the information provided in table 2. The error bars for the cathode discharge parameters (i.e. discharge voltage and current) are evaluated as the standard deviation from the average of seven repeated sweeps acquired under identical operating conditions.

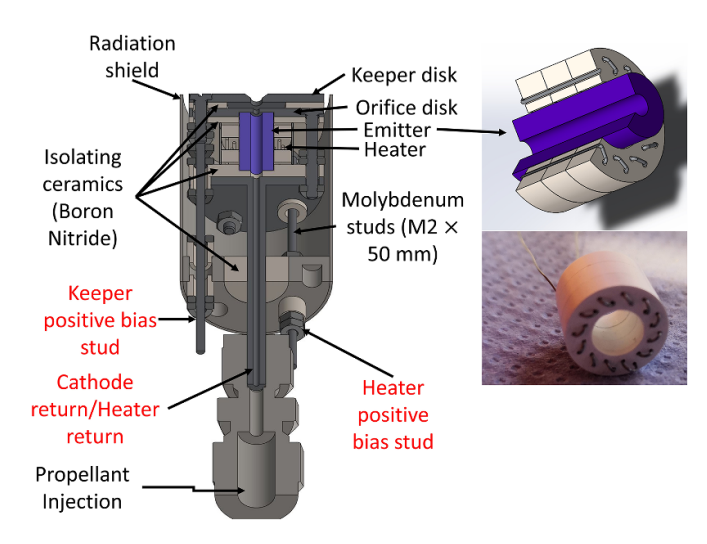


Figure 1. Modular hollow cathode sectional view displaying the internal skeleton.

Table 1. Operational specifications.

Heater ignition power	95–120 W
Keeper ignition voltage Ignition mass flow rate Discharge current Operating mass flow rate	200–250 V 0.3 mg s ⁻¹ Xe or Kr 0.5–4 A 0.1–0.3 mg s ⁻¹ Xe or Kr

2.3. Diagnostics apparatus and setup

2.3.1. Vacuum facility. Standalone experiments are conducted in the Dinko vacuum chamber at the Surrey Space Centre. The chamber (45 cm diameter \times 50 cm length) uses a two-stage pumping system (roughing combined with a turbomolecular pump) with a rated capacity of $3001 \, \mathrm{s}^{-1}$ for nitrogen, achieving a base pressure of $\sim 10^{-6}$ mbar. The pressure sensor used is a Pfeiffer cold cathode IKR 251, the pressure measurements have been corrected for xenon and krypton [25]. For further details, see [8].

Three distinct power supplies are used to operate the modular cathode. The keeper is regulated by a 1.2 kW Programmable Sorensen DC Power Supply, delivering 0 to 300 V and up to 4 A. A Sorensen DLM 40-15 powers the cathode heater, delivering 0 to 40 V and up to 15 A. In triode mode, the anode voltage is controlled by an Aim-TTi CPX200DP power supply, with a voltage range from 0 to 60 V and a current range from 0 to 20 A. The cathode return is electrically isolated from the chamber walls and the cathode-to-ground voltage is measured using a voltmeter. The keeper and anode power supplies are connected to the cathode return, while the mounting interface of the cathode is disconnected. The experimental setup comprising of the vacuum chamber, gas feed system, and power supplies is shown in figure 2. A calibrated MKS 1179 C mass flow controller (full range of 2 mg s⁻¹ for xenon) is used.

2.3.2. OES. OES offers a fast method to gain understanding of the plasma composition qualitatively. The light emitted by the plasma is captured via a lens (Ocean Optics 84-UV-25, nominal focal length of 100 mm) aligned with the symmetry axis of the modular hollow cathode, located downstream of the keeper exit and downstream of the anode. This is shown in figure 3. The OES lens is situated 80 mm from the central hole of the keeper disk, with the line of sight going through a 15 mm diameter opening in the centre of the anode plate.

The intensity of the emission spectrum is measured by an Ocean Optics HR4000CG-UV-NIR spectrometer, with a wavelength range of 200–1100 nm. The integration time is set to 1 second and each spectrum results from averaging 10 acquisitions. A drawback of OES is that the light is collected from the full collection optical volume, which encompasses different plasma regions that might have different properties. Therefore, the measurements are not local. Photon emission from neutrals or ions occurs when an electron impact elevates an atomic electron into a higher energy state, and the electron then transitions to a lower state by emitting radiation corresponding to the energy difference between these levels. Each plasma species has specific emission wavelengths defined for these transitions, typically resulting in distinct, narrow spectral lines. The intensity of these spectral peaks is influenced by multiple factors, including the detector's sensitivity, the ion or neutral density, the electron density and energy, and the excitation cross sections, which depend on the electron energy. The excitation rate coefficient is derived by integrating the electron impact cross sections with the electron energy distribution across different electron energies. The main emission lines observed for neutral xenon are at wavelengths 823.2, 828.0, 834.7 and 881.0 nm, and for single charge xenon ions at 484.4, 529.2, and 541.9 nm [26]. Figures 4 and 5 depict raw OES spectra from two operational configurations. The ratio of amplitudes between the 823 nm and 828 nm wavelengths can serve as an indicator of electron temperature, with the 823 nm neutral line being specifically utilised for this purpose [27]. Additionally, the 529 nm wavelength has been recognised as a representative line for single charge xenon ions in a previous cathode characterisation [28]. However, in our study, OES data is not employed for estimating plasma parameters because Langmuir probe measurements are deemed a more reliable method as the measurements are local. The OES spectra are utilised for a relative qualitative evaluation of xenon neutral and single-charge ion emission under multiple cathode conditions.

2.3.3. Langmuir probe. The Langmuir probe is positioned at a fixed location, 15 mm downstream of the keeper disk along the cathode axis, i.e. at the halfway point of the cathode-anode gap. The probe axis is perpendicular to the cathode axis. This arrangement is illustrated in figure 3.

In the case of a hollow cathode plume operated on xenon, the expected electron density falls within the range of $10^{16} \, \text{m}^{-3}$ to $10^{18} \, \text{m}^{-3}$, while the electron temperature is anticipated to be between 2 eV and 5 eV [1, 7]. The Debye length

 Table 2. Experimental characterisation summary.

Test		Propellant	Mass flow rate (mg s ⁻¹)	Chamber background pressure (mbar)	Keeper Current (A)	Anode Voltage (V)
Standalone	Diode	Xe Kr	0.1–0.3 0.1–0.3	$7.9 \times 10^{-5} - 2.3 \times 10^{-4}$ $9.2 \times 10^{-5} - 2.5 \times 10^{-4}$	0.5–3.5 1.5–3.5	_
	Triode	Xe Kr	0.1-0.3 0.1-0.3	$7.9 \times 10^{-5} - 2.3 \times 10^{-4} 9.2 \times 10^{-5} - 2.5 \times 10^{-4}$	2.5, 3.5 2.5, 3.5	20–50 20–50
Coupled w/XPT	Anode 0.5, 0.8 and 1.0 mg s ^{-1}	Xe	0.1, 0.3	$1.50 \times 10^{-5} - 3 \times 10^{-5}$	2.5	100–300

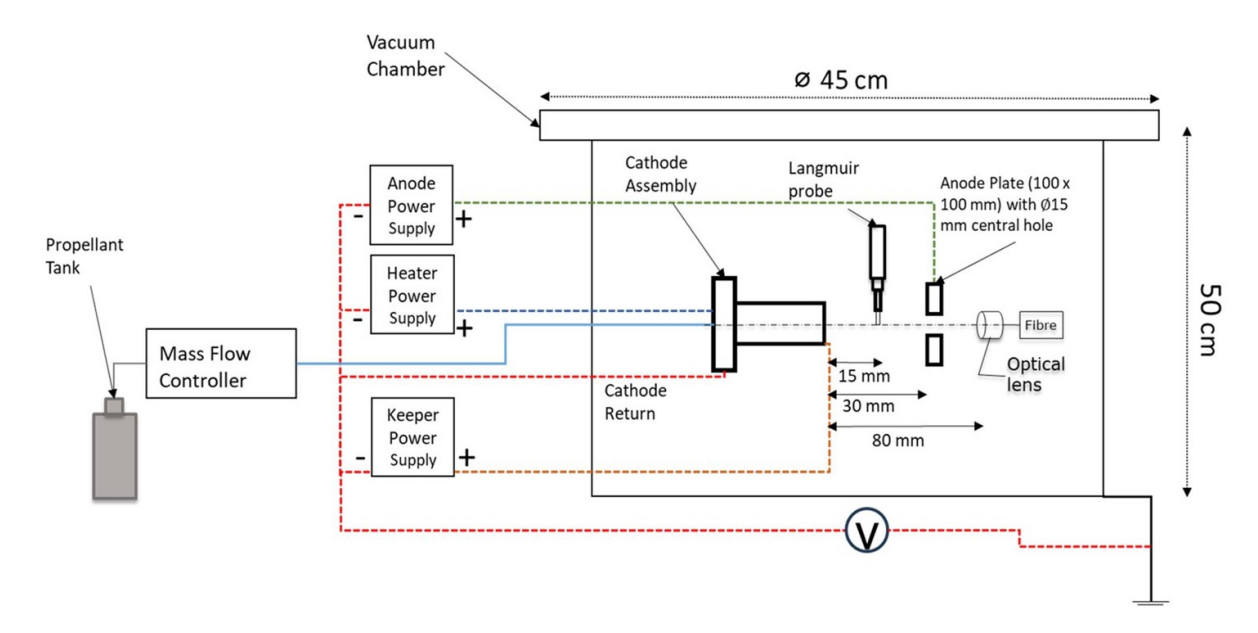


Figure 2. Electrical schematic and setup highlighting the position of the probes, cathode and anode.

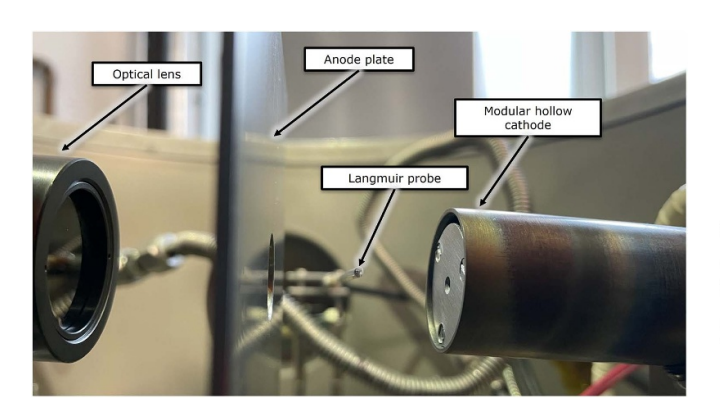


Figure 3. Standalone diagnostics setup showing the optical lens, anode, Langmuir probe and the cathode assembly.

consequently lies within a range of 0.011 mm to 0.166 mm. The cylindrical Langmuir probe tip is constructed from tungsten, with a diameter of 0.375 mm and a length of 2 mm. It is housed within a double-bore alumina tube, where each bore has a diameter (d_p) of 0.6 mm and the outer diameter (D_p), of the tube is 2 mm. The degree of disturbance is verified by the mean free path which should be much larger than the diameter of the ceramic tube, $\lambda_e \gg D_p$ [29, 30]. The neutral density n_n in the cathode plume is predicted to be 1×10^{20} m⁻³, based on a

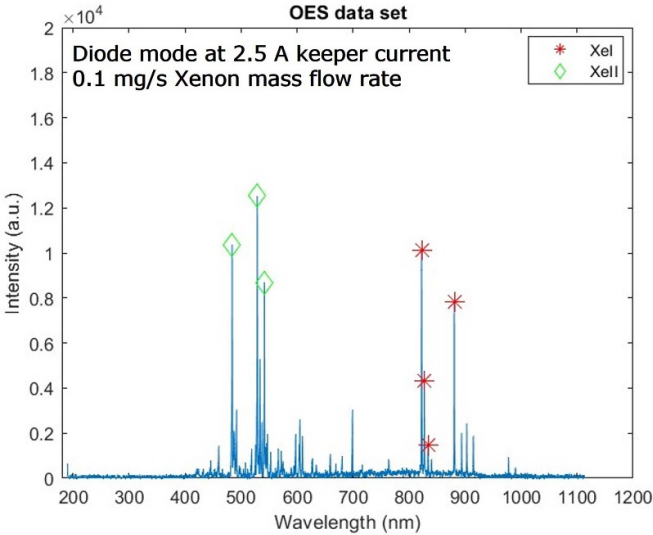


Figure 4. Example of raw optical emission spectra in diode mode.

previous study [28] on a hollow cathode with similar discharge current, orifice size, and xenon mass flow rate. The average electron-neutral elastic collision cross section $\sigma_{\rm en}$ from [31], for xenon is 5×10^{-19} m² and for krypton is 2×10^{-19} m². The

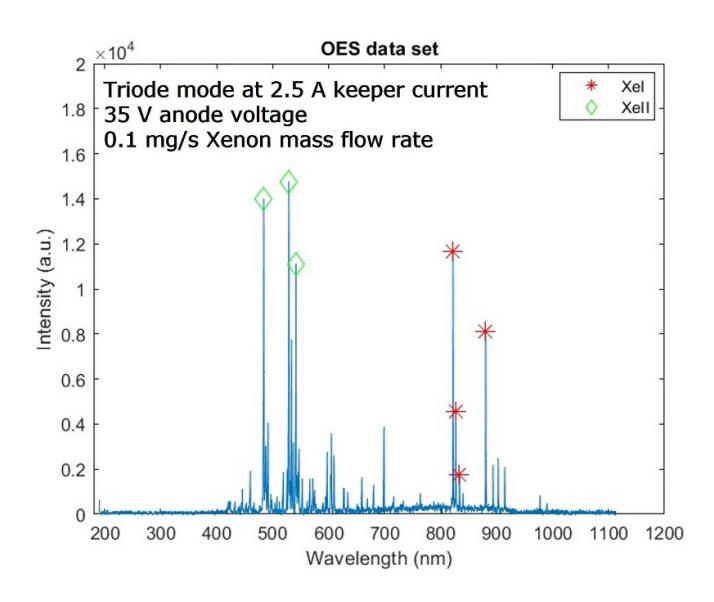


Figure 5. Example of raw optical emission spectra in triode mode.

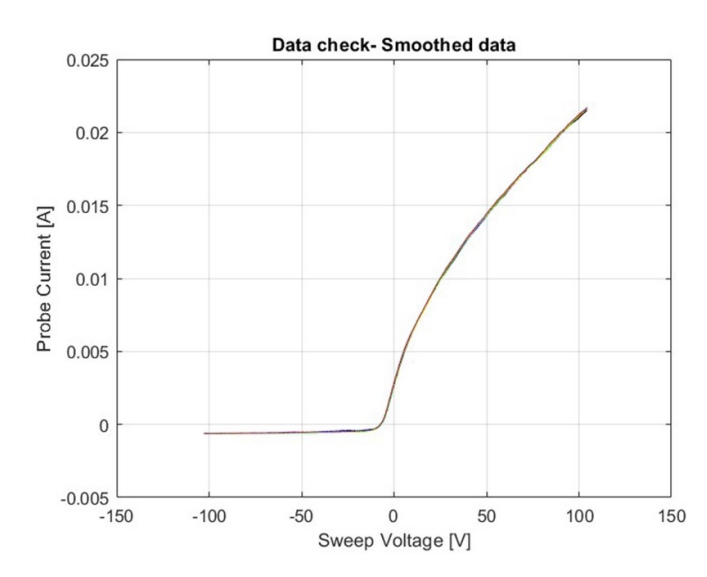


Figure 6. Seven smoothed sweeps for the same operating conditions using the cylindrical Langmuir probe.

mean free path ($\lambda_{\rm e}=(\sqrt{2}n_{\rm n}\sigma_{\rm en})^{-1}$) determined yields a large margin indicating an acceptably low degree of disturbance, as $\lambda_{\rm e}$ for xenon and krypton are 14 and 35 mm, respectively.

The Langmuir probe voltage is swept from $-100\,\mathrm{V}$ to $+100\,\mathrm{V}$ using a KEPCO BOP-500 M bi-polar amplifier (referenced to the common ground of the vacuum chamber), which amplifies the saw-tooth profile provided by a Thandar TG2001 signal generator. The probe current is obtained by measuring the voltage drop across a $100\,\Omega$ shunt resistor, via an Analog Devices AD629 differential amplifier. The voltage drop is recorded using a Rohde & Schwarz RTC1002 oscilloscope ($\pm 3\%$ accuracy of the full scale).

Savitzky–Golay smoothing is employed for processing raw data, using a window of approximately 10^3 points (out of 3.5×10^4 points collected in each sweep) [29]. An example

of data is presented in figure 6. During each acquisition, 7– 8 voltage ramps are performed with the probe, and the resulting plasma parameters are averaged. The error bars hereafter are evaluated as 2σ , where σ is the standard deviation to reflect the consistency of the measurement. However, it is important to note that this reflects the repeatability of the data rather than uncertainties stemming from the assumptions made in the transitional sheath probe theory [32]. The plasma potential is determined using the Druyvesteyn method, which involves identifying the potential at which the first derivative of the probe's current-voltage (I-V) curve reaches its maximum value. The electron temperature (T_e) is calculated by fitting the slope of the natural logarithm of the I-V curve $T_e = (\text{dln}I_e/\text{d}V_{\text{Bias}})^{-1}$ [32]. Based on the transitional sheath probe theory, one can determine the ion saturation current using equation (1) [32],

$$I_{i,\text{sat}}(V_{\text{Bias}}, \lambda_{\text{D}}) = eA_{\text{p}}n_{i}\sqrt{\frac{eT_{\text{e}}}{2\pi M}}a\left(\frac{V_{\text{p}} - V_{\text{Bias}}}{T_{\text{e}}}\right)^{b}$$
(1)

where a is $1.18-0.00080\left(\frac{r_{\rm p}}{\lambda_{\rm D}}\right)^{1.35}$ and b is $0.0684+\left[0.722+0.928\left(\frac{r_{\rm p}}{\lambda_{\rm D}}\right)\right]^{-0.729}$

The electron density, n_e is calculated using the probe current collected $I_{\text{probe}} = I_e + I_{i,\text{sat}}$, the electron saturation current $I_{e,\text{sat}} = I_e(V_{\text{Bias}} = V_p)$, and the fit to the ion saturation current $I_{i,\text{sat}}$ [32]:

$$n_{\rm e} = \frac{I_{\rm e,sat}}{eA_{\rm p}} \sqrt{\frac{2\pi m_{\rm e}}{eT_{\rm e}}},\tag{2}$$

where e is the elementary charge, $r_{\rm p}$ is the probe radius, $A_{\rm p}$ is the probe area, $m_{\rm e}$ is the electron mass, $I_{\rm e}$ is the electron current, $V_{\rm p}$ is the plasma potential, $V_{\rm Bias}$ is the probe bias voltage.

3. Results and discussion

3.1. Diode mode operation

3.1.1. Operational envelope. Initial characterisation of the modular hollow cathode is conducted in diode mode. Ignition is achieved with 250 V applied to the keeper at 0.3 mg s⁻¹ flow rate, limiting the keeper current to 3 A. After ignition, the flow is reduced to $0.1 \,\mathrm{mg}\,\mathrm{s}^{-1}$, the heater is switched off, and the keeper operates in current control mode. Figures 7 and 8 illustrate the operational keeper voltage as the keeper current is swept in 1 A increments from 0.5 to 3.5 A for various flow rates of xenon and krypton. Across all mass flow rates, the patterns observed indicate that as the discharge current decreases, the keeper's discharge voltage rises. The cathode mass flow rate is swept from 0.1 mg s^{-1} to 0.3 mg s^{-1} of xenon and krypton. At 0.5 A keeper current, the keeper voltage is higher when the cathode is operated on krypton in comparison to xenon. As the keeper current increases the keeper voltage decreases to similar magnitudes for both propellants.

3.1.2. Plume properties. It is crucial for the keeper voltage to consistently surpass the plasma potential in the cathode

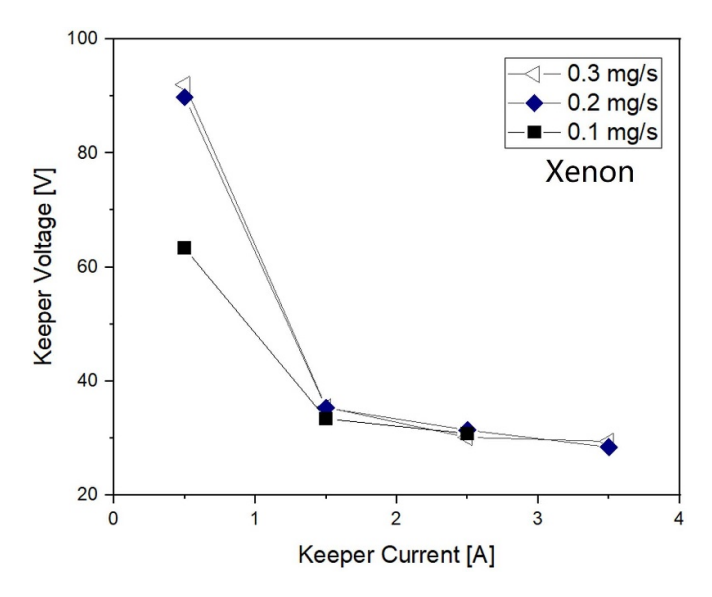


Figure 7. Xenon discharge envelope in diode mode at varying flow rates

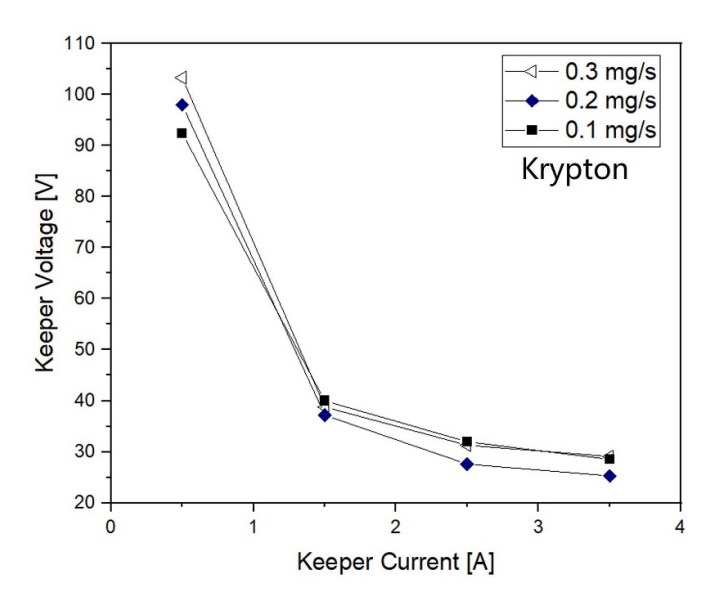


Figure 8. Krypton discharge envelope in diode mode at varying flow rates.

plume to uphold a quasi-neutral plasma within the emitter region, particularly as the sheath surrounding the keeper becomes thinner [10]. As illustrated in figures 9(a) and (b), the plasma potential in the plume downstream of the keeper remains below the keeper voltage for both xenon and krypton, confirming this expectation. At 0.5 A keeper current for all selected mass flow rates on krypton, the cathode discharge is not stable to allow for plume diagnostics to be conducted. This is because the discharge extinguishes after a few minutes when operated without additional heating.

At $0.1~{\rm mg\,s^{-1}}$ of xenon, the electron temperature is measured to be within a range from 2.9 to $4.9\,{\rm eV}$ and the electron density increases from $1.7\!\times\!10^{16}$ to $1.0\!\times\!10^{17}\,{\rm m}^{-3}$ as the keeper current is swept from $0.5~{\rm A}$ to $3.5~{\rm A}$. At the same mass flow rate on krypton, the electron temperature is measured to

be within a range from 4.1 to $4.9\,\mathrm{eV}$ and the electron density increases from 6×10^{16} to $1.4\times10^{17}\,\mathrm{m}^{-3}$ for the same keeper current range. As illustrated in figures 9(e) and (f), the electron density decreases for increasing flow rates at a given keeper current. For xenon operation with $1.5\,\mathrm{A}$ keeper current, the electron temperature presents a sudden higher value and larger standard deviation for the higher flow rate, in contrast with the other keeper current values for which the electron temperature is lower at higher flow rate. This anomaly can be due to a temporary spurious behaviour of the cathode while the measurements were taken.

3.2. Triode mode operation

3.2.1. Operational envelope. An auxiliary positively-biased electrode, a plate with a 15 mm central hole, is placed 30 mm from the keeper and coupled to the modular cathode. The anode is a 100 mm squared stainless steel plate with a thickness of 2 mm. Ignition is initiated at 0.3 mg s^{-1} and 250 V applied to the keeper, with a current limit of 3 A. Once ignited, the flow rate is adjusted to the target, the anode is biased at 50 V, and the keeper switches to current control while the anode is swept in voltage control. Figures 10 and 11 present the results without error bars to enhance trend visibility; however, each data point represents the average of seven repetitions. The typical 2σ interval is approximately 7% of the mean.

This study employs constant voltage discharge to better replicate the operational conditions of plasma thrusters, where the anode voltage is fixed and the cathode adapts to supply the required current. This method enables observing natural plasma changes, like mode transitions, by applying anode voltages beyond the usual beam plasma potential. It complements the methodology of [33, 34], by isolating cathode behaviour in standalone conditions, providing complementary insight into transition dynamics compared to constant current configurations. The lowest anode voltage applied is 20 V and the highest is 45 V. Attempts to operate at 45 V or higher resulted in discharge instability at some operational conditions. Figure 10 illustrates the impact of the keeper current from 1 to 3.5 A, at a constant mass flow rate and auxiliary anode voltage. The keeper voltage-current profile indicates a decreasing discharge impedance as the keeper voltage decreases for increasing keeper current. Figure 11, depicts this behaviour for different values of the anode voltage and 0.1 mg s⁻¹ of xenon.

The modular cathode is subsequently operated on xenon and krypton, sweeping the anode voltage at constant keeper current for mass flow rates values of $0.1\,\mathrm{mg\,s^{-1}}$ to $0.3\,\mathrm{mg\,s^{-1}}$. Figures 12 and 13 show the current–voltage envelopes, indicating a positive discharge impedance across all keeper current settings. A higher keeper current contributes to additional joule heating to the keeper electrode, enhancing emission and resulting in an increased anode current. Specifically, within certain voltage intervals, the anode current for xenon and krypton shows step-like increases. For example, when the anode voltage varies from 30 V to 35 V, the current ranges from $0.3\,\mathrm{A}$ to $1.2\,\mathrm{A}$ at a krypton flow rate of $0.1\,\mathrm{mg\,s^{-1}}$. When the cathode keeper current is maintained at $2.5\,\mathrm{A}$ using xenon and

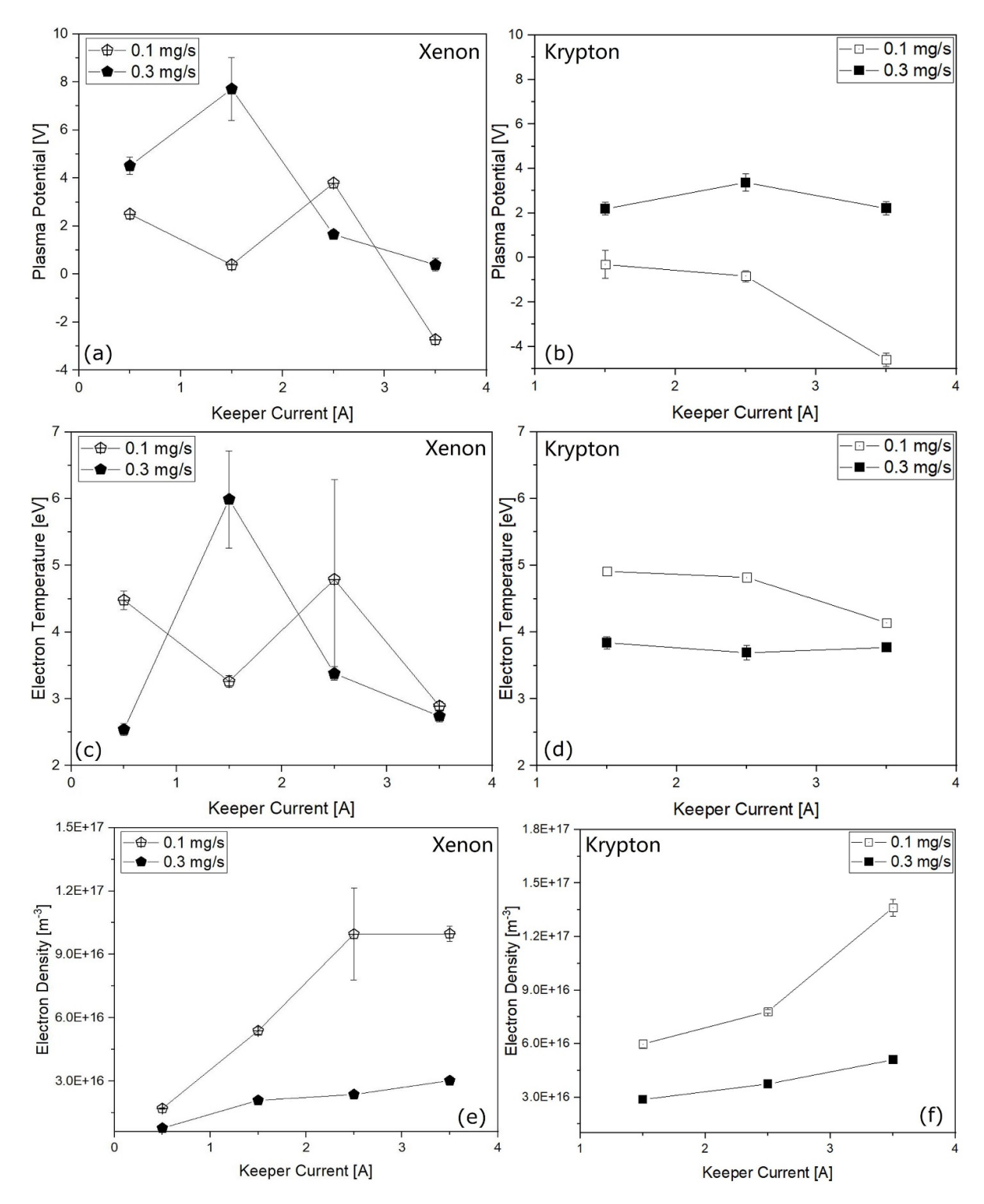


Figure 9. Plasma properties as a function of the keeper current for multiple flow rates of xenon and krypton (a) Plasma potential (xenon). (b) Plasma potential (krypton). (c) Electron temperature (xenon). (d) Electron temperature (krypton). (e) Electron density (xenon). (f) Electron density (krypton).

the anode voltage is increased to $40\,\mathrm{V}$ or higher, the cathode exhibits instability, with oscillations in both keeper voltage and anode current magnitude. The change in plasma properties occurring during this transition is further described in section 3.2.3.

The measured electron temperatures in the cathode plume at stable operating points during the anode voltage sweep range from 3.0 to 4.3 eV for xenon, while for krypton, the range is between 3.7 and 7.3 eV. Figures 14 and 15 compare xenon and krypton discharge properties for a mass flow rate of

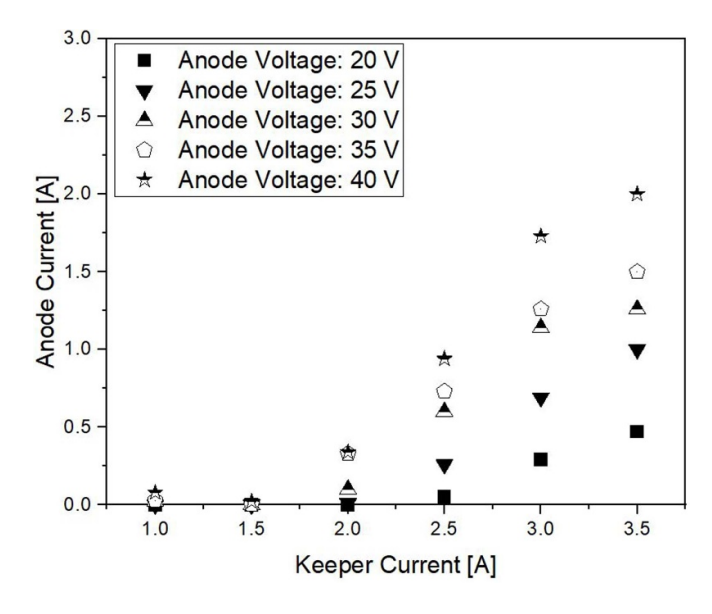


Figure 10. Anode current as a function of the Keeper current for different values of the anode voltage at $0.1 \,\mathrm{mg \, s^{-1}}$ xenon flow rate.

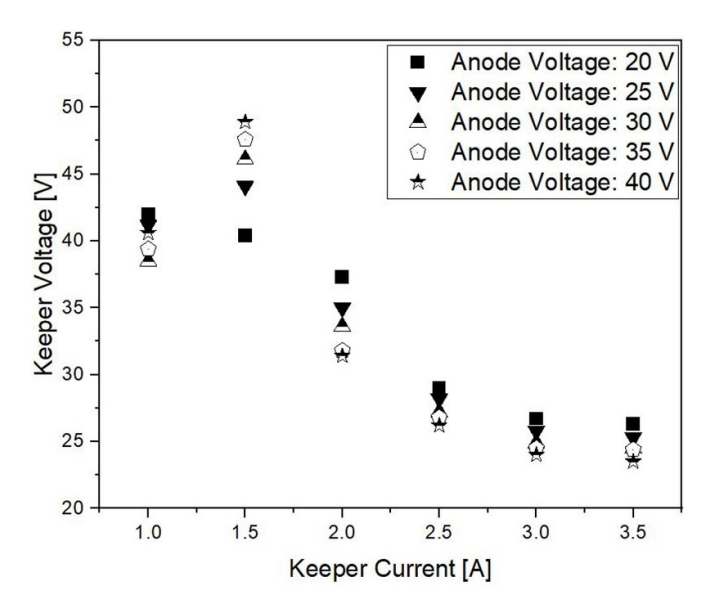


Figure 11. Keeper voltage as a function of the Keeper current for different values of the anode voltage at $0.1 \,\mathrm{mg \, s^{-1}}$ xenon flow rate.

 $0.2 \,\mathrm{mg \, s^{-1}}$. The electron temperatures for xenon are, in general, slightly higher than those for krypton at 1.5 A keeper current, whilst the values at 2.5 A keeper current are approximately the same. Nevertheless, the discharge power of the cathode is notably higher when using krypton compared to xenon on $0.1 \,\mathrm{mg \, s^{-1}}$ and $0.2 \,\mathrm{mg \, s^{-1}}$. The discharge power results from adding the cathode (keeper) power to the anode power. This can be due the lower degree of ionisation for krypton at an equivalent electron energy, since the electron temperature measured in the plume is similar. The rate of ionisation reactions, alongside the ionisation cross section (σ_i) , are affected by the electron temperature. Considering a 15 eV electron energy for both gases [31, 35], the ionisation reaction rate for xenon is five times greater than that for krypton.

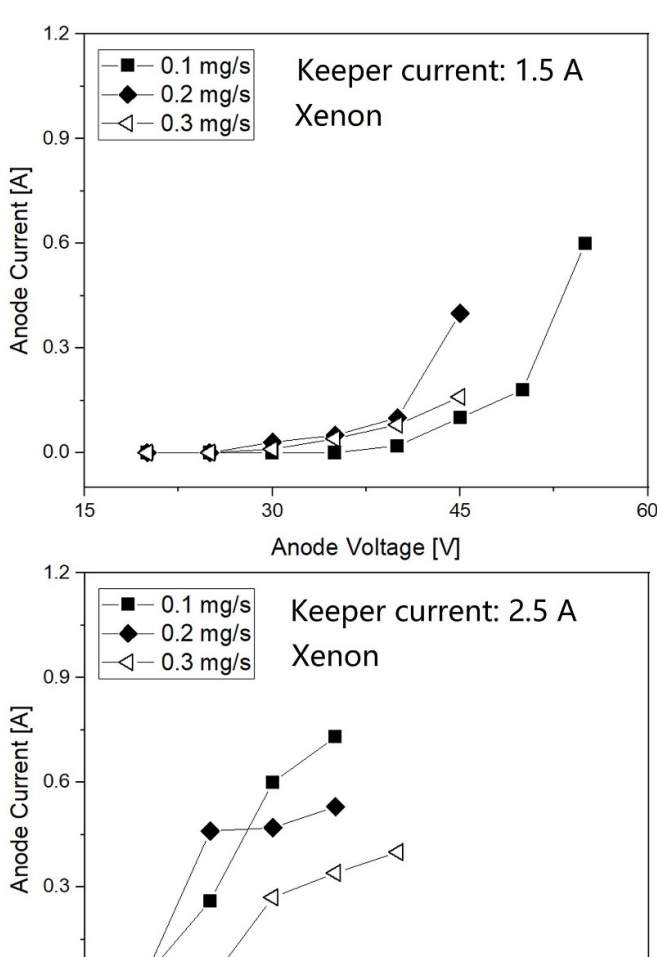


Figure 12. Anode current as a function of the anode voltage at 1.5 A and 2.5 A keeper current and different values of the mass flow rate of xenon.

Anode Voltage [V]

45

60

This may clarify why the cathode (keeper) power is relatively higher during krypton operation at $0.1~{\rm mg~s^{-1}}$ and $0.2~{\rm mg~s^{-1}}$, as the power needed to maintain the internal plasma on krypton rises due to the decreased ionisation reaction rate.

3.2.2. Plume discharge modes. The plume and spot modes are distinct modes of operation influenced by the position of the anode, background pressure, discharge current, plasma density, and electron temperature [9, 12, 36–38]. The spot mode tends to be sustained at a lower plasma potential, lower electron temperature, and higher plasma density in the internal plasma region [15, 17, 38]. The higher plasma density is expected to sustain a passive (thermal) electron current towards the keeper. This is a result of the low electron temperature forming electron attracting sheaths near the keeper [10]. In the case of plume mode the plasma potential increases, resulting in a higher electron temperature and lower plasma density in the internal plasma region.

0.0

15

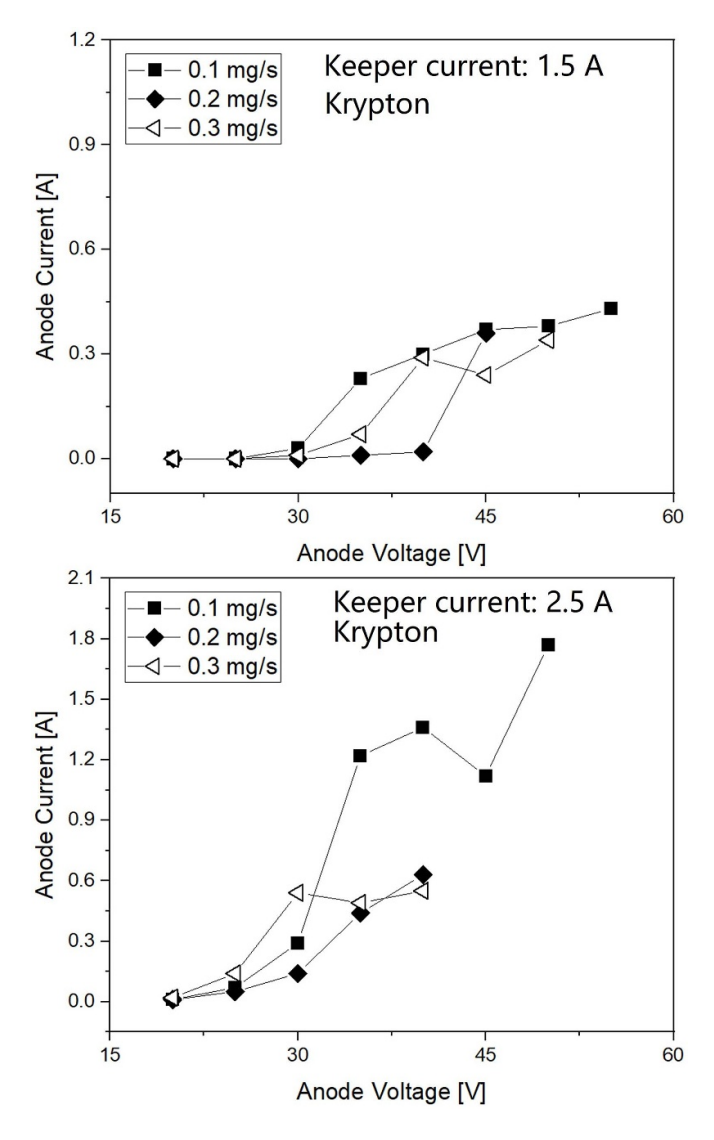


Figure 13. Anode current as a function of the anode voltage at 1.5 A and 2.5 A keeper current and different values of the mass flow rate of krypton.

In the case of the modular hollow cathode all measurements are collected downstream in the keeper-anode region. During spot mode operation, occurring at higher keeper current, lower anode current, and higher mass flow rate, a significant decrease in electron temperature and electron density is observed. Whereas during plume mode, occurring at higher anode currents and lower mass flow rates, a relatively large increase in electron temperature and electron density is observed. Concurrently, due to a higher plasma potential in the keeper region, ion acceleration can be expected to become dominant; this happens especially at lower mass flow rates, i.e. a higher plasma potential leads to a greater negative potential gradient for the ions to fall through to the emitter potential [3]. Unfortunately, this results in ion sputtering of the cathode orifice, discharge instabilities, limited lifetime, and higher coupling voltages. Hence, cathodes are preferably operated in spot mode to mitigate these issues. At higher mass flow rates, the electron pressure is expected to increase significantly

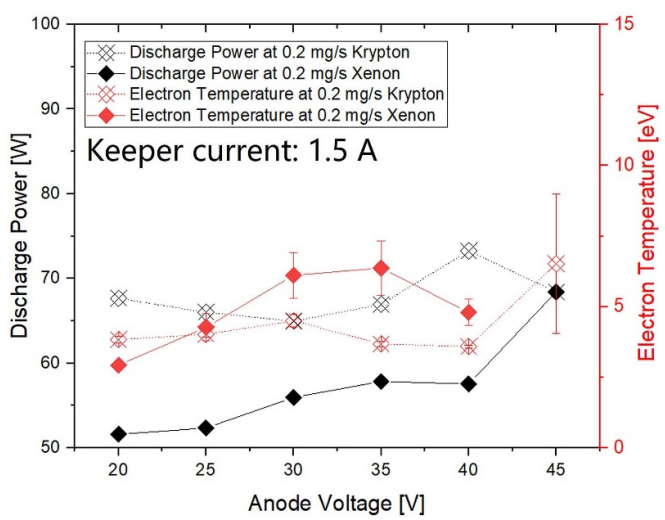


Figure 14. Total discharge power of the modular hollow cathode and electron temperature as a function of the anode voltage for $0.2\,\mathrm{mg\,s^{-1}}$ of xenon and krypton at 1.5 A keeper current.

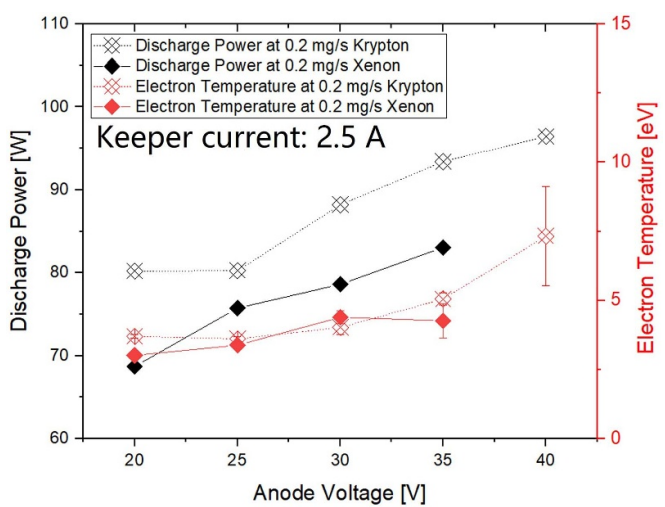


Figure 15. Total discharge power of the modular hollow cathode and electron temperature as a function of the anode voltage for $0.2 \,\mathrm{mg\,s^{-1}}$ of xenon and krypton at 2.5 A keeper current.

within the orifice region which can potentially maintain the spot mode. Figure 16 shows images of the cathode discharge at various operational points.

In this work, three different criteria are used to quantify the spot-to-plume mode transitions: Predatory-prey [39, 40], Kaufman [41] and Rehn–Kaufman criteria [36]. The Kaufman criterion was initially developed to aid in the characterisation of plumes in mercury-fed hollow cathodes [41]. This criterion distinguishes between different plume types by considering the geometric factor of the cathode orifice diameter (d_0) in millimetres, as well as the equivalent mass flow rate measured in equivalent Ampere (A-equiv) [1]. The limits of the Kaufman criterion for plume mode transition can be expressed as 0.14 A-equiv mm⁻¹ $\leq J_0/d_0 \leq 0.4$ A-equiv mm⁻¹ [10, 41]. If ratio values are below 0.14 A-equiv mm⁻¹, a plume or transition mode can be expected. If the ratio lies within the

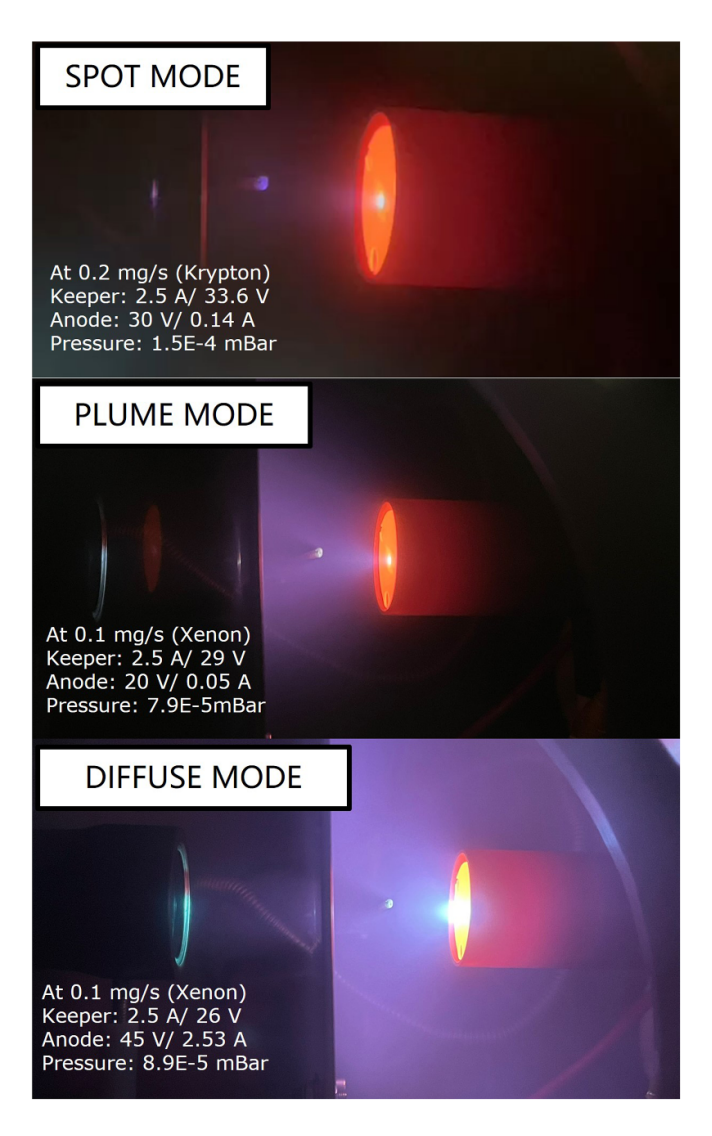


Figure 16. Modular hollow cathode modes of operation. Note: the images are taken with different exposure times.

designated limits plume and spot modes can be expected. This criterion is later modified to the Rehn–Kaufman criterion which accounts for the type of propellant by including the propellant atomic mass (W), and ionisation cross section (σ_i) [10, 36]. According to this empirical criterion, (J_o/d_o) must satisfy the relation (J_o/d_o) × ($\sqrt{W}\sigma_i$) \geqslant 13.9×10⁻²⁰ A-equiv m² amu^{0.5} mm⁻¹ to operate in spot mode and (J_o/d_o) × ($\sqrt{W}\sigma_i$) \leqslant 12×10⁻²⁰ A-equiv m² amu^{0.5} mm⁻¹ to operate in plume mode.

In table 3, the ratios of equivalent mass flow rate to cathode orifice diameter are shown for the modular hollow cathode operated at 2.5 A keeper current, along with the corresponding operational regimes using the Kaufmann and Rhen–Kaufman criteria. The table highlights the plume modes and transitions in operation of the modular hollow cathode using xenon and krypton propellants predicted by those criteria. Based on these estimations, the modular hollow cathode on $0.1 \, \mathrm{mg \, s^{-1}}$ and $0.2 \, \mathrm{mg \, s^{-1}}$ of xenon and krypton is expected to operate in plume mode and as the mass flow rate increases to $0.3 \, \mathrm{mg \, s^{-1}}$

the mode of operation transitions to spot mode. This corresponds well with the experimental findings where at 0.1 mg s^{-1} and 0.2 mg s^{-1} mass flow rates the modular hollow cathode is seen operating in plume mode regardless of the anode current, as shown in figure 16, except for the case on krypton 0.2 mg s^{-1} when the cathode is observed operating in spot mode.

The predatory-prey criterion uses discharge current ($I_{\rm d} = I_{\rm k} + I_{\rm a}$, where the keeper current is $I_{\rm k}$ and the anode current is $I_{\rm a}$) to mass flow rate (\dot{m}) ratios to predict the mode of operation. If the ratio belongs to the interval $1\,{\rm A}\,{\rm sccm}^{-1} < I_{\rm d}/\dot{m} < 10\,{\rm A}\,{\rm sccm}^{-1}$, a plume mode can be expected [10, 14, 42]. The predator-prey criterion is applied to different operating conditions as a function of the anode voltage for multiple mass flow rates of xenon and krypton and different keeper currents. It is observed that the plume mode is no longer consistent at high keeper currents and low mass flow rates for varying values of the anode voltage, and transition into diffuse mode occurs.

If ratio values are below 1 A sccm⁻¹, a transition to spot mode can be expected. For the experimental conditions of this study, the ratio remains below 1 A sccm⁻¹ for xenon operation at a mass flow rate of 0.3 mg s⁻¹. However, for lower mass flow rates, this ratio exceeds 1. A discernible shift in the plume's characteristics occurs for these conditions. Specifically, this shift is observable as the cathode external plasma transforms from a concentrated, 'spotlike' formation at the orifice to a highly divergent plasma, which is recognised as the plume mode [10, 12]. Additionally, at higher anode voltages, the current at the anode increases above the keeper current, inducing the transition from plume to diffuse mode [12]. In the case of krypton, the analysis reveals that at mass flow rates of 0.3 mg s^{-1} and 0.2 mg s^{-1} , the ratio of discharge current to volumetric flow rate consistently remains below 1. At lower flow rates (0.1 mg s^{-1}) , this ratio surpasses the threshold of 1 A sccm⁻¹. In figures 17 and 18, the ratios are plotted as a function of the anode voltage, for multiple keeper currents and mass flow rates. If the experimental observations match the predictions of the predator-prey criterion, a green circle marks the data point; conversely, points where the data do not align are indicated with a red circle.

Figure 17 presents the discharge current to mass flow rate ratio versus anode voltage for various keeper currents at 0.1 mg s⁻¹ xenon mass flow rate. The cathode predominantly operates in plume mode below 3.5 A. As both anode voltage and keeper current increase, a transition to diffuse mode is observed, marked by a sharp rise in anode current and increased chamber luminescence. Due to the lack of oscillation data, this characterisation relies on discharge current trends. It is worth noting that the keeper current appears to have a minimal effect on the spot mode transition. The cathode operates only in plume or diffuse mode, likely limited by total emission current, as 0.1 mg s⁻¹ can yield a low collisionality plasma with high electron temperature, which is known to increase emitter sheath potentials and plasma resistivity, according to previous studies [43].

The experimental results documented in this study reveal that when the ratio of discharge current to volumetric flow

Table 3. Empirical plume criteria estimation for the modular hollow cathode for 2.5 A keeper current, and comparison between theoretical predictions and experimental observations.

	Mass flow rate (mg s ⁻¹)	Kaufman criterion $(\frac{J_0}{d_0})$ $(A - \text{equiv mm}^{-1})$	Rehn-Kaufman criterion $(\frac{J_o \times \sqrt{W}\sigma_i}{d_o})$ (A-equiv m ² amu ^{0.5} mm ⁻¹)	Observed Regime
Xenon (Xe)	0.1 0.2 0.3	0.07—Plume Mode 0.14—Plume Mode 0.21—Spot Mode	4.1×10^{-20} —Plume Mode 8.2×10^{-20} —Plume Mode 1.2×10^{-19} —Spot Mode	PLUME MODE PLUME MODE SPOT MODE
Krypton (Kr)	0.1 0.2 0.3	0.12—Plume Mode 0.23—Spot Mode 0.34—Spot Mode	4.7×10^{-20} —Plume Mode 9.4×10^{-20} —Plume Mode 1.4×10^{-19} —Spot Mode	PLUME MODE SPOT MODE SPOT MODE

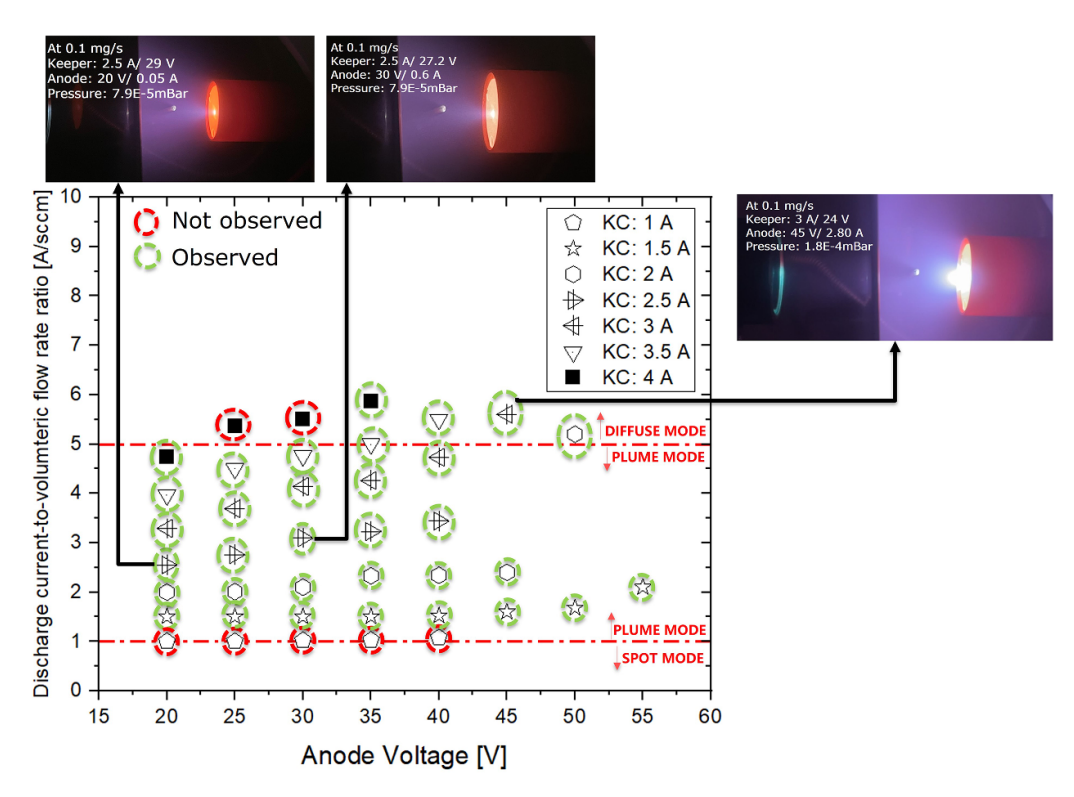


Figure 17. Discharge current to mass flow ratio as a function of the anode voltage for multiple keeper currents and $0.1 \,\mathrm{mg \, s^{-1}}$ xenon mass flow rate. KC in the plot represents keeper current. Green circles confirm experimental observations match with theoretical prediction; conversely, red circles indicate the mismatch between our theoretical prediction and the experimental observations. Note: the images are taken with different exposure times.

rate (I_d/\dot{m}) exceeds 5, a transition from plume mode to diffuse mode generally occurs. Consequently, a value of 5 has been established as the threshold for triggering the diffuse mode in this work. This operational mode can also be seen in the picture embedded in figure 17. At a keeper current of 4 A, the cathode remains in plume mode at anode voltages of 25 V and 30 V, with corresponding anode currents of 1.36 A and 1.50 A, keeper voltages around 24 V, and plasma potentials of 8.10 V and 13.15 V measured 15 mm downstream. When the anode voltage increases to 35 V, the anode current rises to 1.86 A and the plasma potential reaches 22.7 V, matching the keeper voltage (23 V). This alignment triggers a transition to diffuse mode, consistent with conditions where plasma and keeper voltages converge or the plasma potential exceeds the keeper voltage. As previously identified [44], diffuse mode transitions occur when the standard deviations of the discharge voltage waveform exceed 10 V, resulting in a more luminous and divergent plume that expands into the vacuum chamber region. This might suggest that the ionisation and excitation processes are relocating to the far-field plume. In literature [12], during diffuse mode operation, the measurement of the current flow to the vacuum chamber is recommended. Additionally, it is also noted that testing between different facilities at different background pressures can influence the anode current fluctuations, the extension of the plume, and the plasma density, ultimately affecting the cathode operation.

In figure 18, the discharge current to mass flow rate ratio is shown for a wide range of operating conditions as a function of the anode voltage on krypton and xenon. The anode current increases with the voltage applied to the anode for both gases, as represented in figure 14 and 15. The discharge power is higher for krypton, while a lower current is collected by the

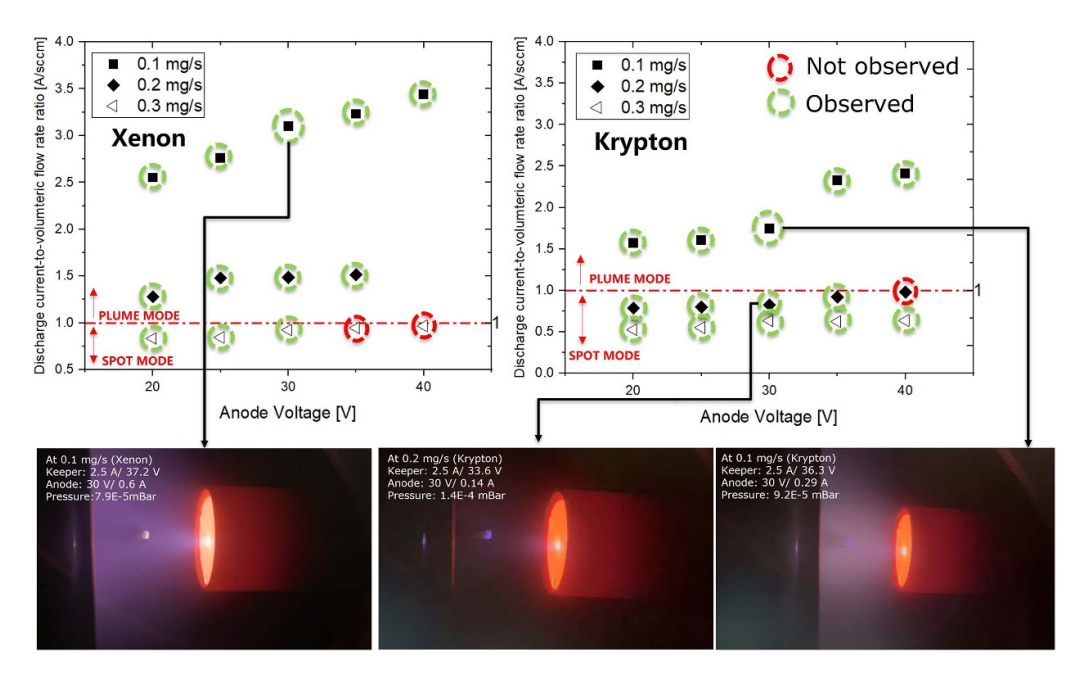


Figure 18. The discharge current to mass flow ratios with increasing anode voltage at varying flow rates of krypton and xenon at 2.5 A keeper current. Green circles confirm experimental observations with theoretical prediction. Note: the images are taken with different exposure times.

anode at an equivalent anode voltage. When comparing the operation of the modular hollow cathode under the same conditions for krypton and xenon, it is observed that at a mass flow rate of $0.2 \,\mathrm{mg}\,\mathrm{s}^{-1}$, the cathode on krypton operates in spot mode as shown in figure 18, while on xenon it is in plume mode. This difference could be due to a lower emission current in the krypton case, indicated by the decreased anode current compared to xenon, which is enough to initiate the transition to spot mode. The ability to achieve spot mode operation at lower flow rates with krypton might be advantageous in certain scenarios, potentially extending the operational lifetime of the cathode. This investigation provides insights into the impacts of the mass flow rate, the anode voltage, and the keeper current on the operational mode of the cathode when using xenon and krypton. This is accomplished through a combination of theoretical forecasts and qualitative experimental evaluations. In general, the operational modes of the modular hollow cathode that are documented and represented in figure 18 generally correspond quite closely to the predator-prey criterion.

The modular hollow cathode is designed primarily for ground testing of plasma thrusters, with a target mass flow rate of $0.1~{\rm mg~s^{-1}}$, corresponding to one-tenth of the thruster's nominal operational mass flow rate. This study suggests that ensuring the cathode's consistent performance, alongside relatively uniform plasma characteristics for different anode voltages, requires minimum mass flow rates of $0.2~{\rm mg~s^{-1}}$ for xenon and $0.3~{\rm mg~s^{-1}}$ for krypton, which are associated with spot mode operation.

3.2.3. External plasma properties. In general, the measurement results show that during operation in spot mode the plasma potential, electron temperature, and electron density

are relatively low. As the cathode operation transitions to plume mode there is a rise in plasma potential, electron temperature, and electron density. There are numerous variables that influence the plasma properties such as background pressure, anode position, and anode current. In this section, the anode voltage and cathode mass flow rate are varied.

The plume characterisation confirms that the plasma potential and electron temperature are influenced by the decrease in the keeper voltage as the keeper current is increased at a constant anode voltage. Figure 19 shows the electron temperature as a function of the keeper current for parametric values of the anode voltage at 0.1 mg s⁻¹ of xenon mass flow rate. As the anode voltage increases, the electron temperature also rises. A greater anode voltage results in a higher potential gradient, which in turn enhances electron acceleration. The current is directly proportional to both the electron density and velocity.

Figure 20 illustrates that when the keeper current exceeds 2.5 A, the electron densities tend to decrease as the anode voltage increases. Hence, the increased anode current shown in figure 10 may result from the higher kinetic energy of electrons. This is because the electron temperature increases with the anode voltage, leading to higher electron velocities. As the anode voltage is raised above 35 V, at 3 and 3.5 A keeper currents, the cathode plume becomes extremely divergent, resulting in an increase in anode current which potentially results in excitation and/or ionisation in the region far from the cathode orifice, as shown in figure 17. The plasma potential and electron temperature measured rapidly increase while the electron density decreases. At 40 V anode voltage, the measured electron density stays relatively constant in the 2.5–3.5 A keeper current range regardless of the change in electron temperature occurring at 3 A. This cathode mode of operation is assumed

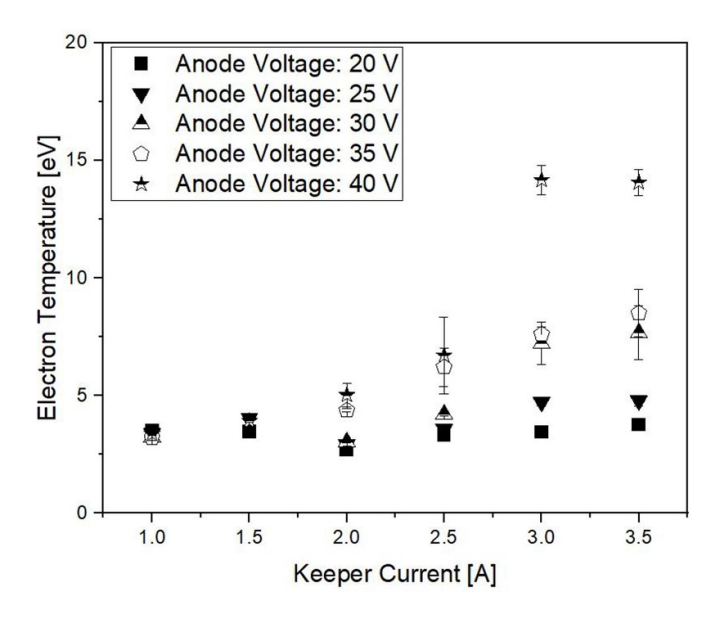


Figure 19. Electron temperature for multiple anode voltages as a function of the keeper current for $0.1~{\rm mg\,s^{-1}}$ xenon flow rate.

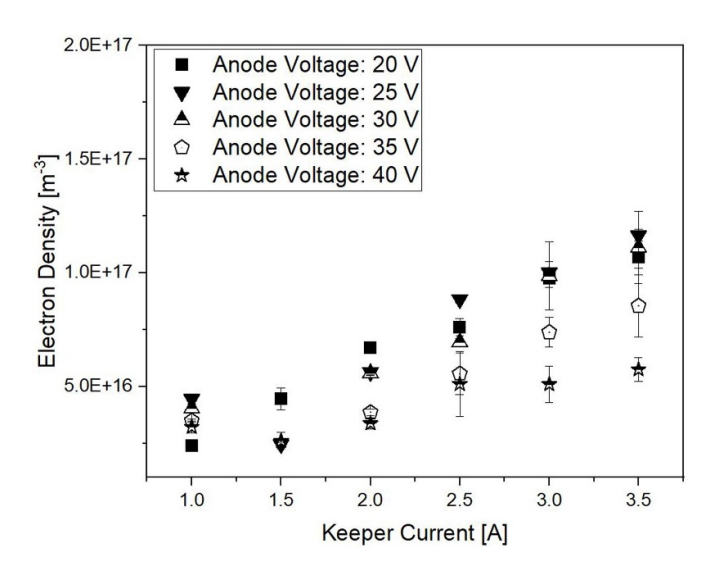


Figure 20. Electron density for multiple anode voltages as a function of the keeper current for $0.1 \,\mathrm{mg\,s^{-1}}$ xenon flow rate.

to be a transition from plume to diffuse, resembling the images shown in figure 16.

In figure 21, the plasma potential, electron temperature, and electron density are presented as a function of the anode voltage for multiple xenon and krypton mass flow rates. Throughout the study, the keeper current remains constant at 2.5 A. The keeper voltage versus the anode voltage for xenon and krypton is depicted in figures 21(a) and (b). As the anode voltage is swept from 20 V to 40 V, the plasma potential increases, which correlates with the electron temperature. In figures 21(c) and (e), at 0.1 mg s⁻¹ xenon mass flow rate operation, an increase in anode voltage leads to a rise in plasma potential and electron temperature. The highest measured plasma potential is 11 V, with an electron temperature of 6.8 eV observed at 40 V anode voltage. For the

0.2 mg s⁻¹ xenon mass flow rate operation, data collection using the Langmuir probe becomes challenging beyond an anode voltage of 35 V due to plume instabilities i.e, variation in the magnitude of the anode current and the keeper voltage. Cathode operation at a 0.3 mg s⁻¹ xenon mass flow rate exhibits significantly greater stability. At this mass flow rate, the plasma potential and electron temperature fall within a similar range as the anode voltage is varied. At an anode voltage of 40 V, the plasma potential is 5 V, and the electron temperature is 3.2 eV. The keeper voltage at 0.3 mg s^{-1} overcomes that at 0.1 and $0.2 \,\mathrm{mg}\,\mathrm{s}^{-1}$. At lower mass flow rates, the energy input per electron may be more significant as the plasma is less collisional, i.e. a limited frequency of electron-neutral collisions at lower mass flow rates allows for a more significant increase in electron energy, and a higher plasma potential as the anode voltage increases, as represented in figures 21(c) and (e). Conversely, the higher mass flow rate results in a higher collision frequency, which can increase energy dissipation and limit the rise in electron acceleration as the anode voltage is increased.

In figures 21(d) and (f), the plasma potential and electron temperature are presented as a function of the anode voltage at multiple mass flow rates of krypton. The keeper voltage versus the anode voltage is also shown in figure 21(b). At 0.1 mg s⁻¹ krypton mass flow rate operation, an increase in anode voltage leads to a rise in plasma potential and electron temperature. The highest recorded plasma potential is 19.3 V, with an electron temperature of 10.2 eV observed at 40 V anode voltage. A notable step-like change of the plasma properties takes place at a krypton flow rate of 0.1 mg s⁻¹, analogous to what has been identified in figure 13 as described earlier. Beyond an anode voltage of 30 V, a transition is observed as the anode current increases from 0.3 A to 1.2 A, as illustrated previously in figure 13. When the anode voltage surpasses 30 V, the plasma potential rises from around 2.5 to 15 V, while the electron density stays nearly constant as shown in figure 21(h). Additionally, the plume becomes highly divergent. At 35 V anode voltage and 0.1 mg s⁻¹ of mass flow rate (plume mode) for krypton, the electron temperature increases from 4.7 eV to 9.2 eV, while the electron density decreases from 8.6×10^{16} m⁻³ to 7.8×10^{16} m⁻³ with respect to operation at 30 V anode voltage. This also corresponds to an increase in anode current and reduction in the keeper voltage. As the mass flow rate is increased to 0.3 mg s^{-1} , a significant shift in plasma potential and electron temperature is recorded. At an anode voltage of 40 V, the plasma potential is 6.3 V with an electron temperature of 4.0 eV. The data highlights the significant impact of the mass flow rate on the plasma properties in the cathode plume. The plasma potential decreases from 19.3 V to 6.3 V, and the electron temperature decreases from $10.2 \,\mathrm{eV}$ to $4.0 \,\mathrm{eV}$ with respect to operation at $0.1 \,\mathrm{mg}\,\mathrm{s}^{-1}$. This indicates that higher mass flow rates result in a more collisional plasma with lower temperatures in the external region between the cathode and anode.

In this configuration, the plasma plume is expanding conically from the keeper to the anode surface. The divergence angle of the plume (θ) is 59^{o} , which in this context refers to the half-angle. The divergence angle is calculated assuming

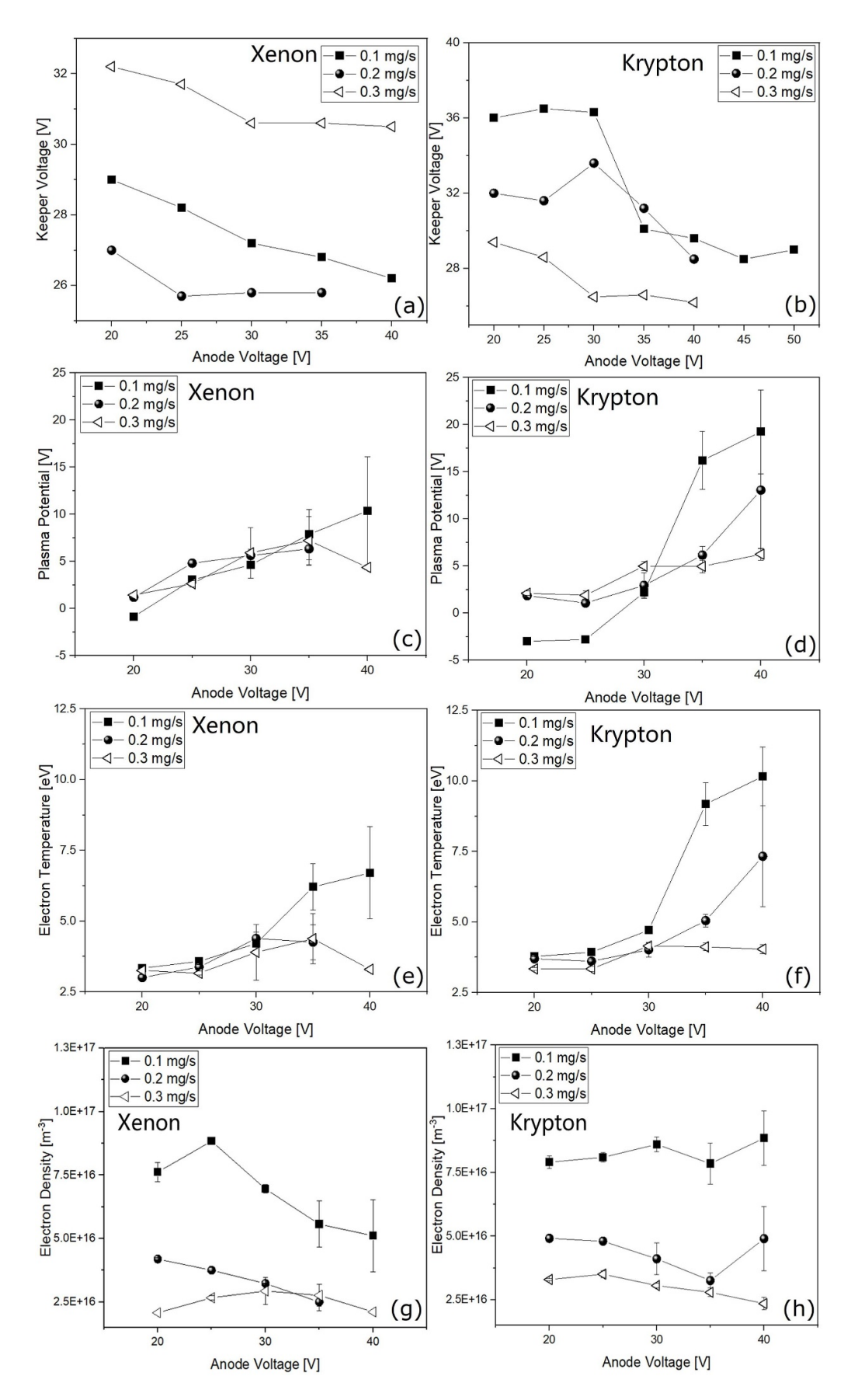


Figure 21. Plasma properties as a function of the anode voltage for multiple flow rates of xenon and krypton at 2.5 A keeper current (a) Keeper voltage (xenon). (b) Keeper voltage (krypton). (c) Plasma potential (xenon). (d) Plasma potential (krypton). (e) Electron temperature (xenon). (f) Electron temperature (krypton). (g) Electron density (xenon). (h) Electron density (krypton).

that the cathode plume stretches from the keeper to the anode and has a width equal to the anode size at the anode axial coordinate [18, 45, 46]. The results for both xenon and krypton quantify the extent of the influence of the mass flow rate on the cathode operating parameters and plume modes, along with the external plasma properties. The collisional environment of the external plasma is strongly dependent on the mass flow rate and the electron-neutral collisional ($\nu_{\rm en}$) frequency, which can be estimated as an additional metric of comparison between the different modes [42, 46]. This study does not directly measure the neutral density in the cathode plume. Instead, an estimation is carried out by utilising the neutral velocity, assuming that the neutral temperature is 10% of the measured electron temperature,

$$\nu_{\rm en} = \sigma_{\rm en} \left(n_{\rm n} - n_{\rm e} \right) \sqrt{\frac{8k_{\rm B}T_{\rm e}}{\pi m_{\rm e}}} \tag{3}$$

$$\sigma_{\rm en}(Xe) = 6.6 \times 10^{-19} \left[\frac{\frac{T_{\rm e}(eV)}{4} - 0.1}{1 + \left(\frac{T_{\rm e}(eV)}{4}\right)^{1.6}} \right]$$
(4)

$$\sigma_{\rm en}(Kr) = 1.08 \times 10^{-19} \left[\frac{\frac{T_{\rm e}(eV)}{3.3} - 0.01}{1 + \left(\frac{T_{\rm e}(eV)}{6.65}\right)^{2.09}} \right]$$
 (5)

$$n_{\rm n} = \frac{\dot{m}}{M v_{\rm n} A_z} \tag{6}$$

$$v_{\rm n} = \sqrt{\frac{8k_{\rm B}T_{\rm g}}{\pi M}} \tag{7}$$

$$A_z = \pi \left[r_k + \tan(\theta) z \right]^2 \tag{8}$$

where A_z is the cathode plume cross sectional area, r_k radius of the keeper orifice, $T_g \approx T_i \approx 0.1 \times T_e$ is the neutral temperature, n_n is the neutral density, θ is the cathode plume divergence angle, z is the axial distance of the probe from the keeper, v_n is the neutral velocity, M is the neutral atom mass $(Xe = 2.18 \times 10^{-25} \text{ kg/Kr} = 1.39 \times 10^{-25} \text{ kg})$, and \dot{m} is mass flow rate. Electron temperatures and densities from Langmuir probe measurements 15 mm from the keeper are used in the calculations.

The chosen mass flow rates, 0.1 mg s⁻¹ and 0.3 mg s⁻¹, correspond respectively to the plume and spot discharge modes of operation, as outlined in section 3.2.2. The estimated neutral density ranges from 3.3×10¹⁹ m⁻³ and 1.0×10²⁰ m⁻³. At a keeper current of 2.5 A and an anode voltage of 25 V for xenon, the electron-neutral collision frequency ranges from 11.7 MHz in plume mode to 33.4 MHz in spot mode. For krypton, the frequency spans from 3.9 MHz in plume mode to 10.8 MHz in spot mode to 10.8 mdz in spot mode, the rate at which electrons in the plasma collide with neutral atoms increases. The higher mass flow rate increases the neutral density which results in a higher collision frequency. In general, the cathode plume plasma for operation on krypton presents a lower electron-neutral collision frequency and approximately equal electron densities compared to those obtained for xenon. The

electron-neutral collision frequency is larger for xenon, confirming that the lighter krypton atoms might experience fewer collisions compared to the heavier xenon atoms due to the smaller electron-neutral cross section, and higher thermal velocities.

3.2.4. Emission spectra results. Neutral (XeI) and single charge ion (XeII) emission lines are identified in the data collected for the modular hollow cathode for xenon. In general, an elevated keeper voltage improves the ionisation rate by increasing the electron temperature, which in turn decreases the neutral density in the internal plasma region. From the measurement using the OES fibre and lens that are in the line of sight of the keeper orifice, relative internal plume emission trends are identified to evaluate the ionisation fraction as the anode voltage and mass flow rate are swept.

In figure 22(a), the ratio of the 529 nm single charge ion line to the 823 nm neutral line is presented in diode configuration as a function of mass flow rate at a keeper current of 2.5 A. In figures 22(b)–(d) the same line ratio is presented in triode configuration as a function of the anode for a keeper current of 2.5 A and multiple mass flow rates. Additionally, xenon spectra in diode configuration (2.5 A keeper current and 0.1 mg s⁻¹ cathode mass flow rate) and triode configuration (35 V anode voltage, 2.5 A keeper current and 0.1 mg s⁻¹ cathode mass flow rate) have been presented earlier in figures 4 and 5. In diode mode, as the mass flow rate is increased, both the neutral line and single charge ion line intensities decrease, with a general decrease of the ion-to-neutral line ratio. However, at $0.1 \,\mathrm{mg}\,\mathrm{s}^{-1}$ and $0.2 \,\mathrm{mg}\,\mathrm{s}^{-1}$ the single charge ion line intensity is greater than that of neutral xenon (line ratio exceeds 1), whereas at $0.3 \,\mathrm{mg}\,\mathrm{s}^{-1}$ the neutral line is the dominant one (line ratio is lower than 1).

At 0.1 mg s⁻¹, the intensity of single charge ion lines increases with anode voltage, with the ion-to-neutral line ratio increasing up to 30 V and then plateauing at higher voltages, as seen in figure 22(b). This potentially suggests a strong effect of the anode voltage on the ionisation fraction of the propellant at the exit plane of the cathode. This trend generally corresponds to the patterns observed in the measurements of the electron temperature, as depicted in figure 22. At 0.2 mg s⁻¹, the 823 nm neutral line is dominant at 20 V anode voltage relative to the 529 nm single charge ion line. However, as the anode voltage increases, the single charge ion line becomes dominant. In the behaviour observed at 0.3 mg s⁻¹ shown in figure 22(d), the 823 nm neutral line shows higher intensity relative to the single charge ion line throughout the full anode voltage range.

In plume mode with a mass flow rate of $0.1 \,\mathrm{mg \, s^{-1}}$, the 529 nm line corresponding to single charge ions becomes more prominent compared to the 823 nm line associated with neutral xenon. Meanwhile, increasing the anode voltage also leads to an increase in the relative ionisation fraction and electron temperature. In spot mode $(0.3 \,\mathrm{mg \, s^{-1}})$, the 823 nm neutral line is dominant relative to the single charge ion line, this is likely due to a plasma species composition with a larger

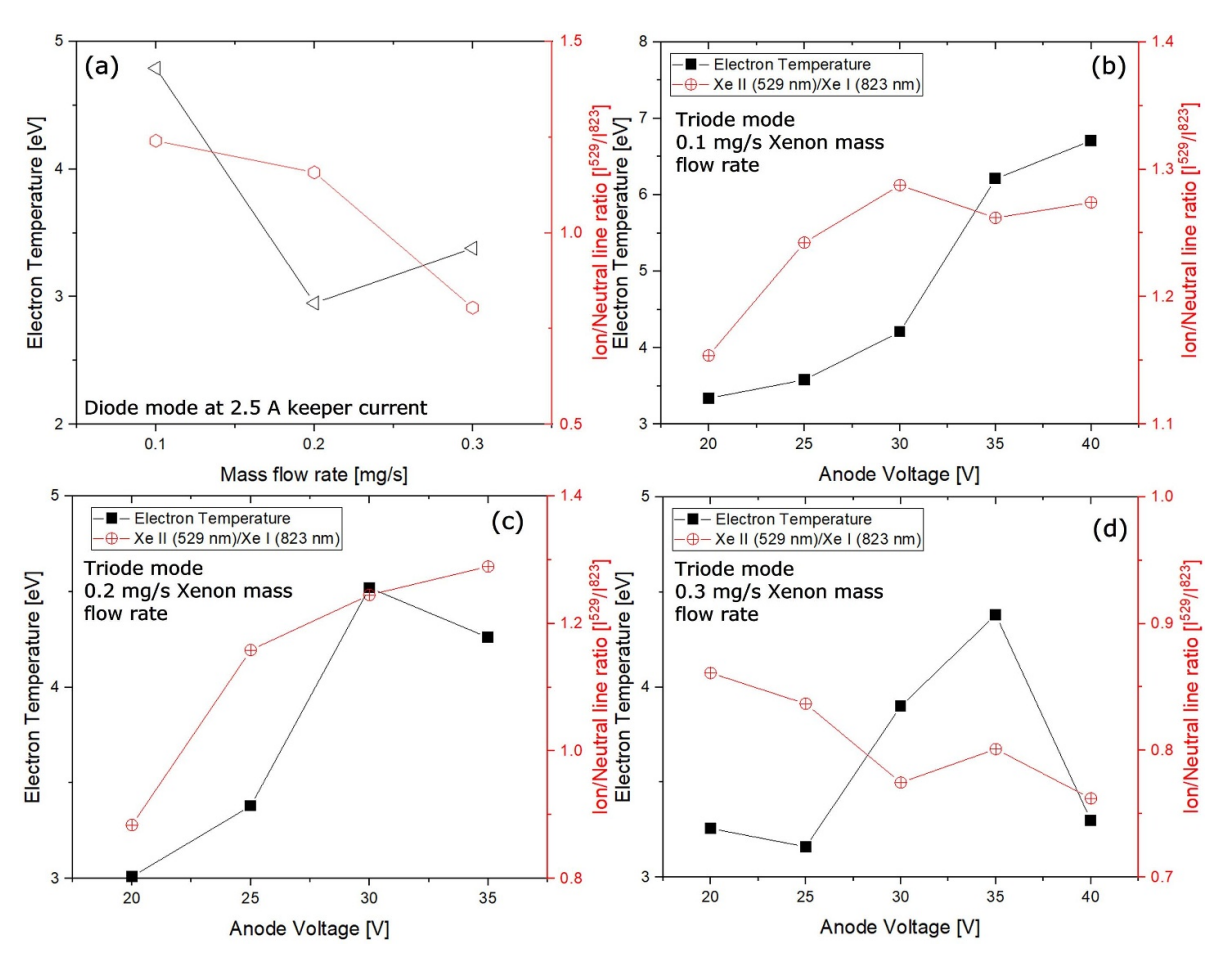


Figure 22. Optical emission line intensity ratio at different operating conditions. (a) Diode mode operation at 2.5 A keeper current as a function of mass flow rate. (b) Triode mode operation at 0.1 mg s^{-1} as a function of anode voltage. (c) Triode mode operation at 0.2 mg s^{-1} as a function of anode voltage.

neutral fraction residing in/leaving from the cathode vicinity when the electron temperatures are much lower, as shown in figure 22. Increasing the anode voltage, in contrast, reduces the relative ionisation fraction. The cathode plasma mode is influenced by the mass flow rate, leading to a more collisional plasma setting with a higher flow rate. Consequently, when the mass flow rate increases from 0.1 mg s⁻¹ to 0.3 mg s⁻¹, the predominant peak transition to 823 nm can be due to increased electron energy dissipation via neutral excitation, in contrast to higher energy electrons at lower mass flow rates, where higher relative ionisation levels are more likely occurring.

3.3. Thruster coupling

The modular hollow cathode is coupled with the XPT, a low-power wall-less hall thruster [47]. The thruster features a cusped magnetic field and produces a thrust level between 0.2 and 10 mN with an anode specific impulse of 150–900 s. The thruster sustains a 'free-space' discharge in front of the anode. This assembly is made of a 34 mm outer diameter ring-shaped anode which is additive manufactured out of stainless steel.

The inner diameter of the anode is 18 mm. The anode cavity is positioned within the thruster chassis and the assembly includes a pair of annular permanent magnets. The magnetic circuit is configured as a magnetic mirror. This leads to a higher magnetic field strength near the anode than in conventional hall thrusters. Hollow cathode electrons are confined in the $\mathbf{E} \times \mathbf{B}$ azimuthal direction. Furthermore, in regions with low potential adjacent to the anode, electrons travelling along magnetic field lines are magnetically reflected back into the bulk plasma, potentially enhancing electron confinement. Additional information on the dimensions of the thruster is reported in [47]. The system is studied with anode power under 400 W and the modular hollow cathode is oriented at a 90° angle relative to the thruster's symmetry axis. The modular hollow cathode is positioned with its orifice at a radius of 70 mm (2 D_A) and an axial distance of 35 mm (1 D_A) from the centre of the anode. Situated near the separatrix, this location likely connects to it via the field lines, improving electron confinement along the magnetic path. The electrical schematic of the set up is shown in figure 23. The coupled tests are carried out within the Daedalus vacuum chamber (1.5 \times 3 m), with a base pressure in the 10^{-6} mbar range, achieved using cryogenic pumps. The performance of the thruster is

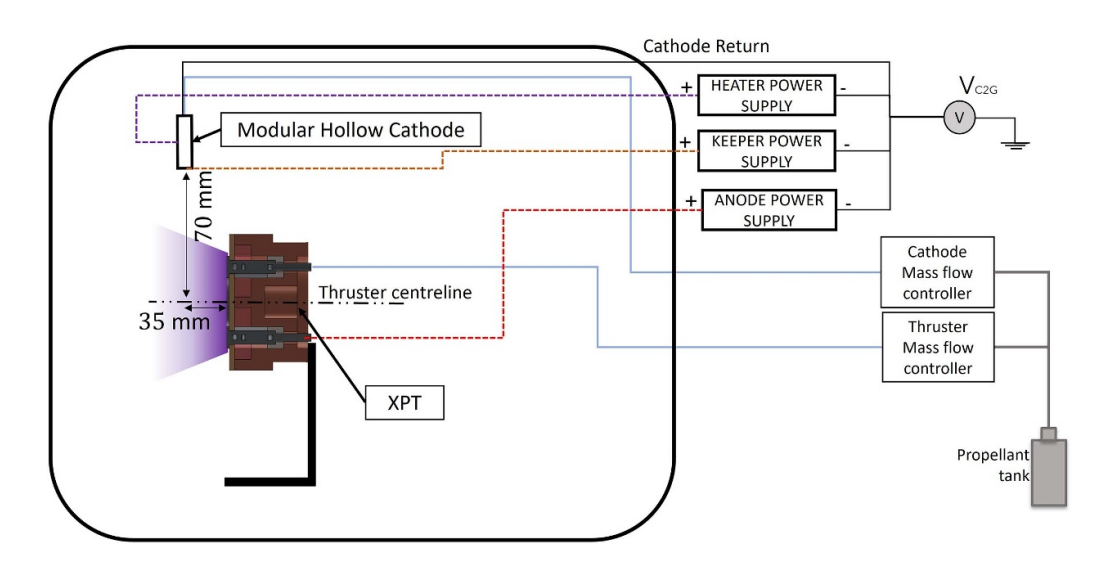


Figure 23. Electrical schematic of the thruster set up in the Daedalus vacuum facility at the Surrey Space Centre.



Figure 24. The XPT operation for multiple anode mass flow rates at a constant cathode mass flow of $0.1 \, \mathrm{mg \, s^{-1}}$, anode voltage of $150 \, \mathrm{V}$ and keeper current of $2.5 \, \mathrm{A}$.

dependent on the operating conditions and position of the hollow cathode [48], influencing both plume composition and the $\mathbf{E} \times \mathbf{B}$ discharge behaviour. The electric field that accelerates ions originates from the potential difference between the anode and the cathode. In this study, the cathode is operated at two different mass flow rates which represent operation in plume mode versus operation in spot mode, investigating the potential implications on the discharge envelope. The keeper current is set to 2.5 A and the cathode mass flow rate is either set to $0.1 \,\mathrm{mg}\,\mathrm{s}^{-1}$ or $0.3 \,\mathrm{mg}\,\mathrm{s}^{-1}$. During the coupling test, the cathode discharge mode was defined based on findings from standalone triode configuration testing presented in section 3.2, rather than visual observation, because of the intense brightness of the thruster. Specifically, previous characterisation showed that at 0.1 mg s⁻¹ the cathode operates in plume mode, and at 0.3 mg s^{-1} in spot mode, allowing mode assignment during coupling based on the known operating conditions. The anode voltage is swept from 100 to 300 V with anode mass flow rates ranging from 0.5 to $1.0 \,\mathrm{mg \, s^{-1}}$. In figure 24, the thruster plasma discharge is shown for different mass flow rates at a constant anode voltage of 150 V,

a keeper current of 2.5 A, and a cathode mass flow rate of 0.1 mg s^{-1} .

The background pressure range at a cathode mass flow rate of $0.1\,\mathrm{mg\,s^{-1}}$, as the anode mass flow rate is swept from $0.5\,\mathrm{mg\,s^{-1}}$ to $1.0\,\mathrm{mg\,s^{-1}}$, is between $1.38\times10^{-5}\,\mathrm{mbar}$ to $2.89\times10^{-5}\,\mathrm{mbar}$. As the cathode mass flow rate increases to $0.3\,\mathrm{mg\,s^{-1}}$, the pressure level increases to between $1.50\times10^{-5}\,\mathrm{mbar}$ and $2.93\times10^{-5}\,\mathrm{mbar}$. Changing the background pressure is expected to have a substantial effect on the thruster; in particular, this affects the ionisation and acceleration processes and near-field plume structure. This could be vitally important for thrusters with wall-less configurations.

In figures 25(a) and (b), the keeper voltage at $0.3~{\rm mg~s^{-1}}$ cathode mass flow rate (spot mode), has a much lower value compared to the $0.1~{\rm mg~s^{-1}}$ operation (plume mode). The anode current shows an increase at a cathode mass flow rate of $0.3~{\rm mg~s^{-1}}$, a pattern that remains consistent across all chosen anode mass flow rates. The keeper voltage decreases by approximately 15 % as the cathode mass flow rate is increased from $0.1~{\rm mg~s^{-1}}$ to $0.3~{\rm mg~s^{-1}}$ and the anode current increases by approximately 8 %. Figures 26(a) and (b) illustrate the

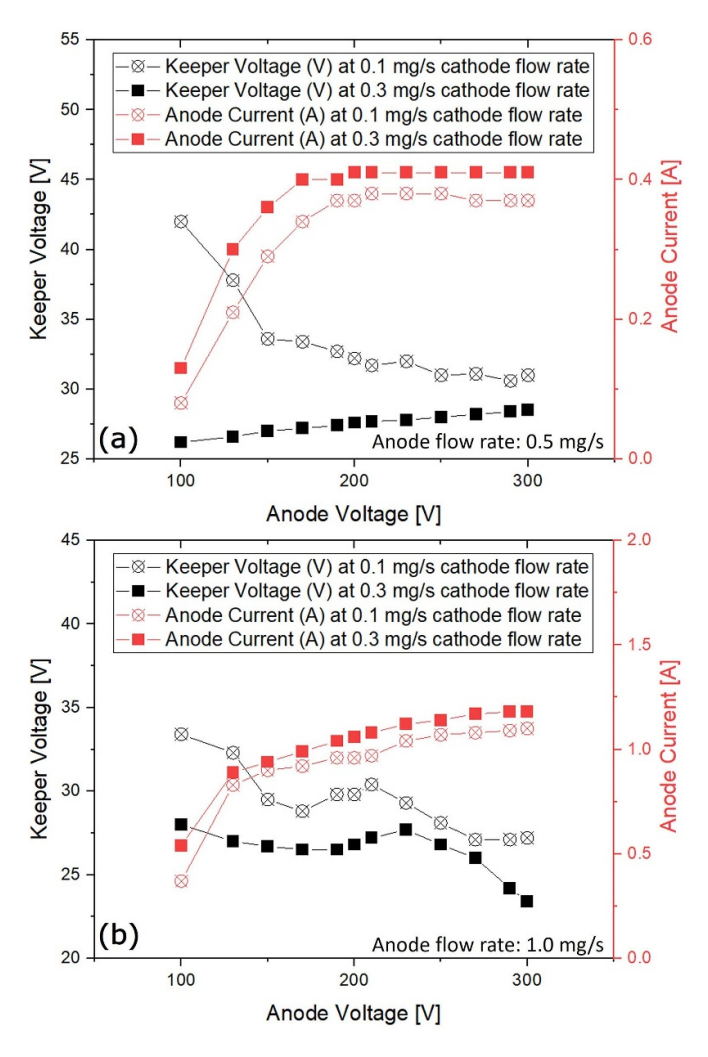


Figure 25. Keeper voltage and anode current as function of anode voltage for $0.1\,\mathrm{mg\,s^{-1}}$ and $0.3\,\mathrm{mg\,s^{-1}}$ cathode flow rate (a) at $0.5\,\mathrm{mg\,s^{-1}}$ anode mass flow rate (b) at $1.0\,\mathrm{mg\,s^{-1}}$ anode mass flow rate.

cathode-to-ground voltage plotted versus the anode voltage at anode mass flow rates of $0.5 \,\mathrm{mg \, s^{-1}}$ and $1.0 \,\mathrm{mg \, s^{-1}}$. The cathode-to-ground voltage in plume mode is much higher in magnitude (more negative) than that in spot mode. Operation at higher cathode to ground voltage magnitudes (more negative values) has been shown to impede the performance of these types of thrusters [6, 34, 49], i.e. improved cathode electron emission in spot mode potentially contributes to improved thruster performance. Additionally, the increased cathode mass flow rate results in a higher neutral density in the plasma discharge. Injecting extra propellant from the cathode might change the local neutral density, possibly affecting the discharge operation significantly, i.e. increasing the anode current.

4. Conclusion

This work characterises the modes of operation of a modular hollow cathode and determines the external plasma properties

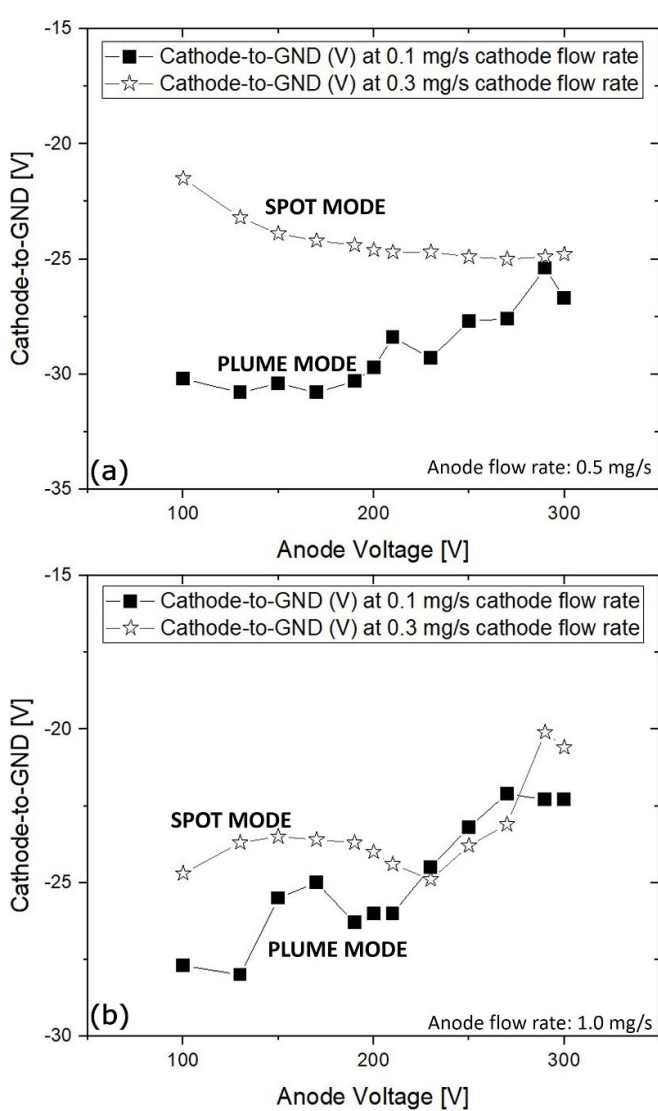


Figure 26. Comparison between the cathode-to-ground voltage profiles as a function of the anode voltage obtained for two different cathode mass flow rates $(0.1~{\rm mg~s^{-1}}~{\rm and}~0.3~{\rm mg~s^{-1}})$ (a) at $0.5~{\rm mg~s^{-1}}$ anode mass flow rate (b) at $1.0~{\rm mg~s^{-1}}$ anode mass flow rate.

using invasive and non-invasive diagnostic techniques in standalone testing (diode and triode configurations) using xenon and krypton. In addition, a thruster-coupled characterisation is presented. The key findings are summarised as follows.

- (i) The plasma characteristics of the modular hollow cathode in diode configuration are studied as a function of the keeper current and the mass flow rate. The findings indicate that a higher mass flow rate decreases both electron temperature and density, whereas a higher keeper current increases the electron density.
- (ii) The plasma properties in triode configuration are examined for multiple keeper currents as a function of the anode voltage and cathode mass flow rate. As the mass flow rate increases from 0.1 to 0.3 mg s⁻¹, a decrease

- in plasma potential, electron temperature, and electron density is observed as a function of the increasing anode voltage, and this similarly correlates to the current collected on the anode.
- (iii) Plasma diagnostics are used to characterise the operational modes of the modular hollow cathode across varying mass flow rates, highlighting transitions from plume mode to spot mode (or vice versa). As the mass flow rate increases, a shift towards spot mode is observed, accompanied by the increasing collisionality, which is reflected in variations in the electron temperatures and corresponding trends of the Xe neutral/ion line ratios from the optical emission spectra.
- (iv) The transition to diffuse mode has also been identified when the collected current on the anode exceeds the constant keeper current and the plasma potential exceeds the keeper voltage, observed at approximately 5 A sccm⁻¹ for the modular hollow cathode. The experimental observations align with the theoretical predictions using various criteria (Predatory-prey, Kaufman and Rehn-Kaufman criteria).
- (v) The coupling of the modular hollow cathode with a non-traditional external discharge hall-effect thruster is shown, showcasing stable operation and delivering an anode current ranging from 0.3 to 1.2 A at a cathode mass flow rate of 0.1 mg s⁻¹ and 0.3 mg s⁻¹ on xenon with keeper power of 87 W and 67 W, respectively.

Data availability statement

All data that support the findings of this study are included within the article.

Acknowledgments

M Ahmed thanks the University of Surrey for his PhD scholarship funding. The authors would like to thank the Propulsion Lab Technical Support and Mechanical Engineering Workshop teams at Surrey, particularly Brian Eades and Jonathan Stacey.

References

- [1] Goebel D M and Katz I 2008 Fundamentals of Electric Propulsion: Ion and Hall Thrusters 1st edn (Wiley)
- [2] Lev D, Mikellides I, Pedrini D, Goebel D, Jorns B and Mcdonald M 2019 Plasma Phys. 3 6
- [3] Goebel D M, Jameson K K, Katz I and Mikellides I G 2007 Phys. Plasmas 14 103508
- [4] Farnell C C, Williams J D and Farnell C C 2011 Plasma Sources Sci. Technol. 20 025006
- [5] Meng T, Ning Z and Yu D 2019 Phys. Plasmas 26 093510
- [6] Meng T, Qiao C, Wang Y, Ning Z and Yu D 2020 Vacuum 172 109040
- [7] Tian F, Miao L, Xia Q, Liang F, Wang N and Hou X 2023 Acta Astronaut. 211 130–41

- [8] Ahmed M, Karadag B, Masillo S and Lucca Fabris A 2024 Vacuum 219 112653
- [9] Potrivitu G C, Mazouffre S, Grimaud L and Joussot R 2019 Phys. Plasmas 26 113506
- [10] Potrivitu G C, Xu L, Huang S, Rohaizat M W A and Xu S 2020 J. Appl. Phys. 127 064501
- [11] Oshio Y, Kubota K, Watanabe H, Cho S, Ohkawa Y and Funaki I 2019 *JSASS Aerosp. Tech.* **17** 203–10
- [12] Sakai S, Katayama T, Aoyagi J and Takegahara H 2007 Discharge modes and characteristics of hollow cathode Proc. 30th Int. Electric Propulsion Conf.
- [13] Mooney M M, Baird M and Lemmer K 2019 Featherweight heaterless hollow cathode characterization *Proc. 36th Int. Electric Propulsion Conf.*
- [14] Georgin M P, Jorns B A and Gallimore A D 2017 An experimental and theoretical study of hollow cathode plume mode oscillations *Proc. 35th Int. Electric Propulsion Conf.*
- [15] Mazouffre S, Joussot R, Vincent B and Tsikata S 2021 J. Appl. Phys. 130 173301
- [16] Mikellides I G and Katz I 2008 J. Propuls. Power 24 855-65
- [17] Goebel D M, Becatti G, Mikellides I G and Lopez O A 2021 J. Appl. Phys. 130 050902
- [18] Potrivitu G and Xu S 2022 CEAS Space J. 15 729-49
- [19] Lim J W M et al 2019 Plasma Sources Sci. Technol. **28** 064003
- [20] Liu Y, Ren J, Cao S, Zhang G, Zhang Z and Tang H 2020 J. Phys. D: Appl. Phys. 53 425205
- [21] Qin Y, Xie K, Guo N, Zhang Z, Zhang C, Gu Z, Zhang Y, Jiang Z and Ouyang J 2017 Acta Astronaut. 134 265–77
- [22] Wang F F, Meng T H, Yu D R, Ning Z X and Zhu X M 2022 J. Phys. D: Appl. Phys. 55 455202
- [23] Karadag B, Cho S, Funaki I, Hamada Y and Komurasaki K 2018 J. Propuls. Power 34 1094–6
- [24] Karadag B, Cho S and Funaki I 2018 *J. Appl. Phys.* **123** 153302
- [25] Dankanich J W, Walker M, Swiatek M W and Yim J T 2017 J. Propuls. Power 33 668–80
- [26] Nist xenon energy levels (available at: https://physics.nist.gov/ PhysRefData/Handbook/tables/xenontable2.htm (Accessed 20 March 2023)
- [27] Karabadzhak G F, Chiu Y-H and Dressler R A 2006 J. Appl. Phys. 99 113305
- [28] Ahmed R I M 2003 Physics of hollow cathode breakdown and steady-state operation with several inert gas propellants *PhD Thesis* University of Southampton
- [29] Caldarelli A, Filleul F, Boswell R W, Charles C, Rattenbury N J and Cater J E 2023 Phys. Plasmas 30 040501
- [30] Tisaev M, Karadag B, Masillo S and Lucca Fabris A 2023 J. Appl. Phys. 134 193302
- [31] Bordage M C, Biagi S F, Alves L L, Bartschat K, Chowdhury S, Pitchford L C, Hagelaar G J M, Morgan W L, Puech V and Zatsarinny O 2013 J. Phys. D: Appl. Phys. 46 334003
- [32] Lobbia R B and Beal B E 2017 J. Propuls. Power 33 566–81
- [33] Li J, Zhou L, Hu Y, Fan H, Ma H, Wei L and Ding Y 2024 J. Phys. D: Appl. Phys. 57 375207
- [34] Goebel D M, Jameson K K and Hofer R R 2012 *J. Propuls. Power* **28** 355–63
- [35] Rapp D and Englander-Golden P 1965 J. Chem. Phys. 43 1464–79
- [36] Rehn L and Kaufman H Correlation of inert gas hollow cathode performance (available at: https://arc.aiaa.org/doi/ abs/10.2514/6.1978-707)
- [37] Ning Z, Chu Y, Liu X, Li F, Zhu X and Yu D 2019 Plasma Sci. Technol. 21 125402
- [38] Potrivitu G C, Joussot R and Mazouffre S 2018 *Vacuum* 151 122–32

- [39] Csiky G A 1969 Measurements of some properties of a discharge from a hollow cathode Other NASA Technical Note (TN) (NTRS- NASA Technical Report Server)
- [40] Williams G, Smith T, Domonkos M, Gallimore A and Drake R 2000 *IEEE Trans. Plasma Sci.* **28** 1664–75
- [41] Kaufman H R 1975 Technology of Electron-Bombardment ion Thrusters (Advances in Electronics and Electron Physics) vol 36, ed L Marton (Academic) pp 265–373
- [42] Georgin M P, Jorns B A and Gallimore A D 2020 *Plasma Sources Sci. Technol.* **29** 105010
- [43] Potrivitu G C, Xu L and Xu S 2021 Plasma Sources Sci. Technol. 30 085012
- [44] Oshio Y, Kubota K, Watanabe H, Cho S, Ohkawa Y and Funaki I 2017 Experimental investigation of lab6

- hollow cathode with radiative heater *Trans. JSASS Aerospace Tech. Japan, Vol. 17, No. 2, pp. 203-210, 2019*
- [45] Ito T and Cappelli M A 2009 Appl. Phys. Lett. **94** 211501
- [46] Potrivitu G and Xu S 2022 J. Electr. Propuls. 16
- [47] Ahmed M and Lucca Fabris A 2024 Plume characterisation of a low power external discharge plasma thruster 38th Int. Electric Propulsion Conf.
- [48] Raitses Y, Granstedt E, Smirnov A, Merino E and Fisch N 2008 44th AIAA/ASME/SAE/ASEE Joint Propulsion Conf. and Exhibit
- [49] Sommerville J D and King L B 2011 *J. Propuls. Power* **27** 744–53